Assimilation of Transformed Retrievals from Satellite High-Resolution Infrared Data over the Central Pacific Area

Tiziana Cherubini[a] Paolo Antonelli[b], Steven Businger[a] and Paolo Scaccia [b]

[a] *Mauna Kea Weather Center, University of Hawaii - Dept. of Atmospheric Sciences, Honolulu, HI/USA*

[b] *AdaptiveMeteo S.r.l., Roma, Italy*

Corresponding author: Tiziana Cherubini, tiziana@hawaii.edu

ABSTRACT

A month-long data assimilation experiment is carried out to assess the impact of CrIS and IASI Transformed Retrievals (TRs) on the accuracy of analyses and forecasts from a 3-h Weather Research and Forecasting (WRF) cycling system implemented over the central North Pacific Ocean. Conventional observations and satellite MicroWave (MW) radiance data are assimilated along with TRs in comparative experiments. Both the NCEP Global Forecasting System (GFS) and the European Centre for Medium-Range Weather Forecasts (ECMWF) analyses are used in the evaluation process. The results show that the assimilation of TRs, both alone, and in combination with MW radiance assimilation, have the greatest impact on the characterization of the moisture field in the middle atmospheric levels (800 to 300 hPa), and particularly in the lower portion (800 to 600 hPa). The latter improvement is likely due to a refinement in the vertical definition of the trade-wind inversion.

1. Introduction

This paper presents the results of an assessment on the impact of the assimilation of Transformed Retrievals (TRs) into the Weather Research and Forecasting (WRF) modeling system during a month-long experiment over the Central North Pacific Area. Transformed Retrievals represent a very efficient method for exploiting the information content of hyperspectral satellite data (Migliorini et al. 2008; Migliorini 2012). This work is an extension of the study by Antonelli et al. (2020; A2020 hereafter) where TRs were generated using ‘‘Mirto’’ 1DVAR (Antonelli et al. 2017) and ingested into a modified version of the WRF model (Skamarock et al. 2008), with 3DVAR data assimilation (WRFDA; Barker et al. 2004, 2012). Preliminary results in A2020 were encouraging and showed a positive impact on the characterization of the water vapor distribution, and a decrease in the root mean square error (RMS) of the 3-h accumulated precipitation forecasts for the record-breaking Kauai flood event (Corrigan and Businger 2021). These preliminary results from a limited case study prompted the present more comprehensive assessment study.

Assimilation of TRs has many advantages: (i) it is akin to assimilation of physical profiles, but overcomes the errors introduced by using an *a priori* knowledge of the atmospheric state in the physical retrieval process (Eyre, 2007; Eyre et al. 2019); (ii) the Mirto approach is fundamentally more efficient in processing thousands of wavelengths available from hyperspectral instruments than direct assimilation of radiant energy of each of these thousands of wavelengths, moreover, only a subset of the available wavelengths are used in operational radiance assimilation; (iii) TRs are independent of the characteristics of the hyperspectral instruments and the observation operator, unlike for direct radiance assimilation, comes with the TRs; (iv) the Mirto approach also allows wavelengths corresponding to, for example, ozone and carbon dioxide to be included in the calculations, providing an accurate and focused solution, whereas wavelengths sensitive to, for example, methane and sulfur dioxide and others that are hard to model are excluded from the calculations.

Since Antonelli et al. (2017), the retrieval processor, Mirto, was refined and extended to be able to retrieve profiles above the cloud top. This greatly expands the TRs assimilation potential in cloudy regions such as higher latitudes in winter. Assimilation of TRs above the cloud top is a subject for future work and is not included in this study.

The current investigation expands the research reported in A2020 in two ways: i) includes a month-long assimilation experiment that allows for robust forecast statistics; and ii)

independently assimilates MicroWave (MW) radiance observations into the WRFDA system (Barker et al., 2004, 2012). The MW emissions from atmospheric water vapor provide an independent and complimentary data set. Because MW frequencies can pass through non-precipitating clouds, they provide complementary observations, albeit at lower spectral resolution, over cloud covered regions where TRs are unable to at this stage. This work was conducted at the Mauna Kea Weather Center (MKWC) in Hawaii. The MKWC is a weather research and forecast facility funded by the astronomical observatories on Mauna Kea (Businger et al. 2002; Cherubini et al. 2011; Lyman et al. 2020; Cherubini et al. 2021; http://mkwc.ifa.hawaii.edu), and routinely runs the WRF Model system.

Studies demonstrated that assimilating MW radiances with variational DA algorithms improves forecasts in global numerical weather prediction (NWP) models over areas with few conventional observations (Simmons and Hollingsworth 2002; Zapotocny et al. 2008) and in limited area NWP models when using variational data assimilation systems (Wang et al. 2021). However, the successful direct assimilation of MW radiances, as with any satellite radiances in limited-area models, is very challenging. It requires the use of a radiative transfer model, observation thinning, a good understanding of the limits and potentials of the sensors/channels involved, and, most of all, bias correction (Dee 2005; Auligné, et al. 2007; Auligné and McNally 2007; Auligné 2007). The latter can be cumbersome and challenging to implement, especially in limited-area models, due to the non-uniform coverage of polar orbiting satellites. In contrast, TR assimilation into a limited-area model like WRF is straightforward, from the user perspective, because it eliminates the need for a radiative transfer model. Once the NWP model is equipped with a dedicated assimilation module, minimal parameters tuning is needed, as most of the sensor-related parameters are handled by the retrieval processor (Mirto). While direct radiance assimilation of hyperspectral sensors with thousands of channels requires the understanding and tuning of many parameters, the retrieval process compresses all the underlying physical information into a very limited number of parameters (< 20 eigenvectors), provides an *ad hoc* observation operator, and reduces the observation error covariance to the Identity Matrix regardless of the hyperspectral sensor's characteristics, thus limiting the amount of tuning needed by the users at assimilation time. The present study also shows that TR assimilation does not seem to require bias correction, as TR assimilation is ultimately more comparable to single profile assimilation than radiance assimilation.

Three parallel experiments were designed to evaluate the impact of assimilating TRs and the combined assimilation of TR and MW radiances in a WRF 3-h cycling system on the

system's nowcasting and forecasting accuracy. Each experiment produces analyses every 3 hours between 0300 UTC 20 November and 1200 UTC 18 December 2020. These analyses initialize 12-h WRF forecasts. The GFS and ECMWF analyses, available at synoptic times, are used to validate the WRF predictions.

This paper is structured as follows: section 2 provides the working framework in terms of the description of the involved models' configurations and the observational data availability; section 3 describes the experiments design and section 4 the adopted validation strategies; and results are presented in section 5. Conclusions and future work are outlined in section 6.

2. Model set up and data availability

The underlying working framework used in this study is partially described in section 2 of A2020. The chosen WRF model configuration encompasses the domain in Fig. 1 of A2020, with horizontal grids spacing of 4500 m centered over the north-central Pacific area and the island of Hawai'i, which correspond to the coarser and parent domain in the MKWC operational configuration (A2020 and Table 1). A custom adaptation of the WRF Data Assimilation system version 3.9.1, which includes modules to assimilate TR, is used in this study (Antonelli et al. 2015; A2020; DeHann et al. 2015). The WRFDA is capable of ingesting a wide variety of observation types. The different datasets used in the assimilation experiments in this study are described hereafter.

Table 1: WRF configuration

Domain parameters			
E-W n of grid points	N-S n of grid points	$\Delta x = \Delta y$ [km]	Integration time step
451	451	4500	30s
Map Projection	Mercator		
Physical Packages			
Microphysics	WRF Single-Moment 6-class microphysics scheme which allows for ice, snow and graupel (Hong and Lim 2006)		
Cumulus	Tiedtke cumulus convention scheme (Zhang and Wang 2017)		
PBL	Mellor-Yamada-Janjic (MYJ) Planetary Boundary Layer scheme (Janjic 2002)		
Radiation	RRTM longwave-shortwave radiation scheme (Mlawer et al. 1997; Dudhia 1989)		
Land surface	Noah Land Surface Model (https://ral.ucar.edu/solutions/products/noah-multiparameterization-land-surface-model-noah-mp-lsm)		
Surface Layer	Eta similarity surface layer scheme (as used in Eta Model).		

a. Conventional Observations

In data assimilation experiments, in-situ observations are the classical and most commonly used type of data. They include conventional radiosondes as well as ground and upper air observations. Only two radiosondes are available in the Central Pacific Area: Hilo (PHTO, 91285) and Lihue (PHLI, 91165) radiosondes. Other conventional observations include: METAR, SYNOP, ship and buoy for ground observations; and TEMP, AIREP, ACARS, TAMDAR for upper air observations. The WRFDA is also capable of assimilating some remote sensing derived products. Among these, Atmospheric Motion Vectors (AMV; Cherubini et al. 2006) and QuickScat winds are present in the data used in this study. For the sake of simplicity, we refer to them as "Conventional Observations" (CO) throughout this paper (National Centers for Environmental Prediction, NCEP/NWS/NOAA/U.S. Department of Commerce, 2008). This dataset is the output from the final step of the NCEP Global Forecasting System (GFS) Data Assimilation System (GDAS), which prepares the majority of conventional observational data for assimilation into various NCEP analyses. A certain level of quality control is already performed to this dataset before making it available. WRFDA is capable of ingesting these data "as is" with no pre-processing necessary. Figure 1 shows examples of the typical geographical distribution of available conventional observations.

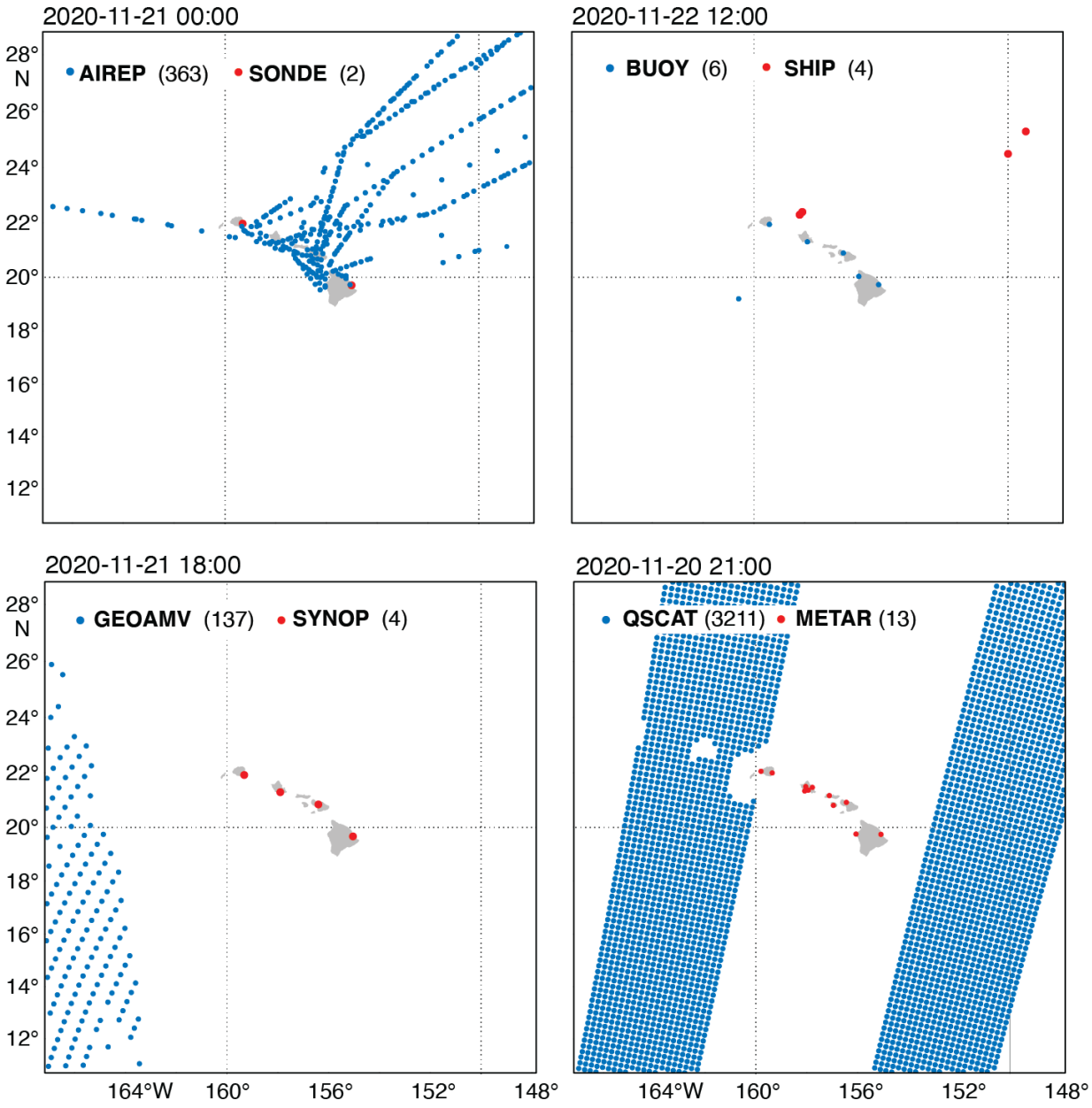

Fig. 1: Examples of the spatial distribution of conventional observations available from the Global Data Assimilation System.

b. Transformed Retrievals

Level 1 data from both the CrIS and IASI sensors on *Suomi NPP* and *NOAA-20,* and *MetOp-A/B/C* for the period from November 20th to December 31st, 2020 were fed to the Mirto processor (Antonelli et al. 2017), which produced 1DVAR physical retrievals of temperature and relative humidity, instability indices, and TRs, along with their observation

operators for the entire timeframe. The TRs and their corresponding observation operators are the quantities used in the assimilation process within the modified WRFDA system (A2020). Although the version of Mirto under development is capable of retrieving information on cloudy-sky conditions also, only retrievals in clear-sky conditions are included in this study. The impact of assimilating TRs above cloud top is left for future investigations.

An example of the distribution of clear-sky fields of view (FOVs) associated with successful Mirto retrievals is provided in Fig. 2. This distribution is obtained by patching together the CrIS data from adjacent *Suomi-NPP* overpasses that overlap the model domain and occur during the 2-h windows centered at 1200 UTC on December 1st, 2020. The aggregated data for each overpass are quality controlled and then thinned to 80 km. The performed quality control is described in A2020.

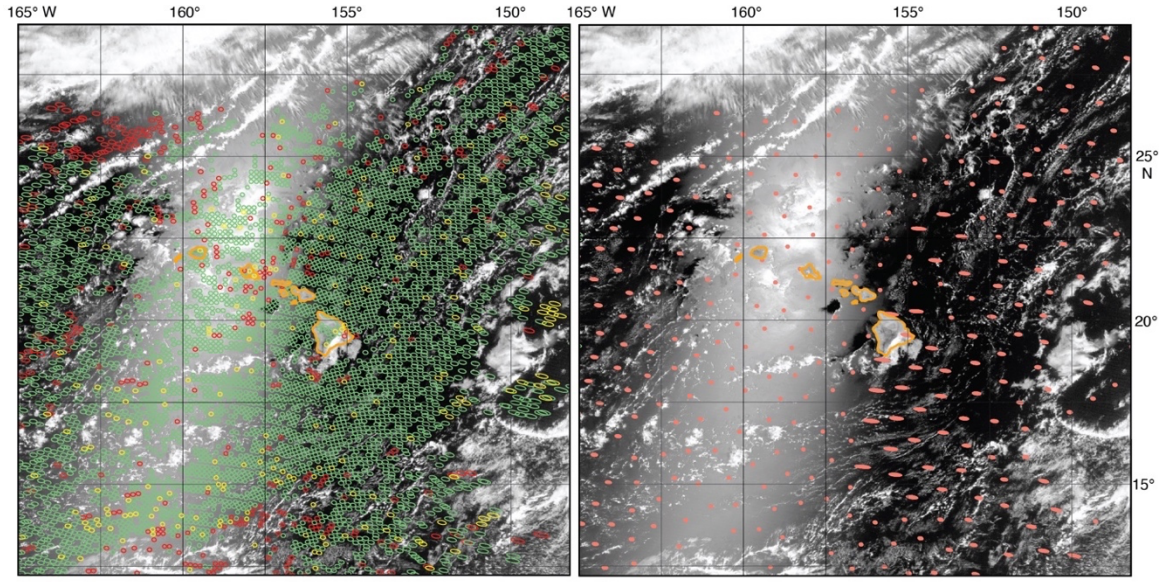

Fig. 2: Locations of convergent, non-saturated CrIS retrievals (RH < 100% for any level) obtained from two adjacent *Suomi-NPP* overpasses, before (a) and after (b) the 80 km thinning is applied. Data are overlaid on a VIIRS true color image valid for 0000 UTC 01 December.

The TRs are assimilated in WRFDA by an adapted version of the original satellite radiance module (A2020, section 3b). The TR observation operators are characterized by at most 20 eigenvectors of the Signal to Noise matrix (Migliorini et al. 2008; Migliorini 2012). In the current WRFDA implementation only eigenvectors associated with eigenvalues of the signal to noise matrix greater than 1 are retained. Due to refinements of the a-priori covariance matrix in Mirto, 15 of the available 20 eigenvalues are actively assimilated (versus 12 over 20 of the previous study). The TRs used in the experiment timeframe consistently show that the bulk of the information from the underlying hyperspectral sensors is carried by the first 15 eigenvectors

(Fig. 3). Within WRFDA, eigenvector selection for TR works just like channel selection for radiance assimilation[1]. A quality control (QC) is implemented within the assimilation module that rejects any normalized observation whose difference with the background is outside the 3-σ confidence interval (A2020). In the current configuration of Mirto and the WRFDA module for TR assimilation no bias correction scheme has been implemented. Although bias correction is very relevant for radiance assimilation experiments to be successful (Eyre 2016), our results seem to suggest that there is no need for bias correction in TR assimilation (see section 3).

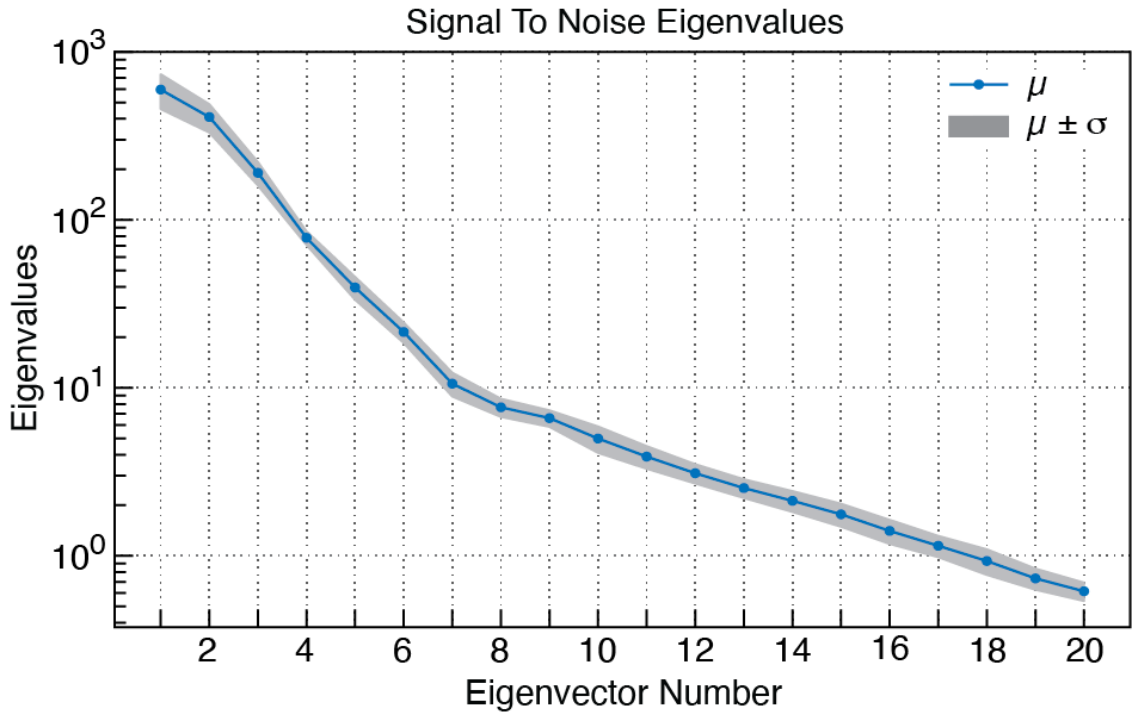

Fig. 3: Logarithmic distribution of eigenvalues (mean and standard deviation) of the signal-to-noise matrix (Eq. 7 in A2020) for 01 December 2020 at 1200 UTC. Three hundred thirty-three IASI FOVs with 3306 channels per FOV were assimilated. The eigenvalues larger than 1, are those that actually carry significant information about the true state vector.

c. MicroWave Radiances

The microwave radiances used are from: (i) Advanced Microwave Sounding Units A (AMSU-A) on board of various satellite systems (Aqua, METOP-A/B, NOAA18/19), which has 15 channels in the microwave range; (ii) Microwave Humidity Sounder (MHS), which has five channels in the MW range, on board the NOAA-18/19 and METOP-A/B; (iii) Advanced Technology Microwave Sounder (ATMS), which currently flies on the *Suomi NPP* and

[1] https://www2.mmm.ucar.edu/wrf/users/wrfda/Docs/radiance_userguide_v1.pdf, page 6

NOAA-20 satellite missions and senses the atmosphere through 22 channels. These sensors, which observe the Earth in the MW portion of the electromagnetic spectrum, can "see" through clouds. Although available, the *MetOP-C* MW radiance data are not used in this study because assimilation capability is only implemented from WRFDA version 4.3. Table 1 summarizes the sensors included in the assimilation and also indicates which channels are actively assimilated. Only channels active in the default set up of the WRFDA are used here. Sensitivity tests for the number of channels used is beyond the scope of this study[2]. IASI and CrIS radiance data are not included in this experiment to avoid the same information content being assimilated twice. However, IASI and CrIS radiance data could be present in the initial conditions of the cold-start cycles because the GFS fields are the results of the NCEP GDAS, which assimilates radiances from these sensors. Moreover, only radiance data in the MW range is included, as it is believed to provide information complementary to that from hyperspectral sensors.

Table 2: Assimilated radiances

Satellite ID	Sensor	Channels
NOAA-18/19	MHS	3,4,5
EOS-Aqua	AMSU-A	5,6,8,9
NOAA-18/19	AMSU-A	5,6,7,8,9
MetOP-A/B	AMSU-A	5,6,7,8,9
MetOP-A/B	MHS	3,4,5
Suomi NPP	ATMS	6,7,8,9,10, 18,19,20,21,22

3. Experiment set up

The WRF modeling system can run in cold-start mode, which uses the NCEP GFS analyses and forecast as initial and boundary conditions, or in cycling/hot-start mode, where each

[2] More can be found in terms of channel quality at:
www.emc.ncep.noaa.gov/mmb/data_processing/Satellite_Historical_Documentation.htm

forecast cycle is initialized using the forecast from the previous cycle as background, and a custom analysis is created by ingesting available local observations in WRFDA. A 3-h cycling frequency is used and the WRF forecasting system is refreshed with a cold-start run every three days. Whether in cold-start or cycling mode, each forecast is 12-h-long for the purpose of this study. Each forecast is kept short to limit the amount of output data given the long experiment timeframe. Moreover, at this stage, the focus is on the analyses and early simulation hours, which are the ones likely to carry the largest effect from the assimilation process as described in A2020.

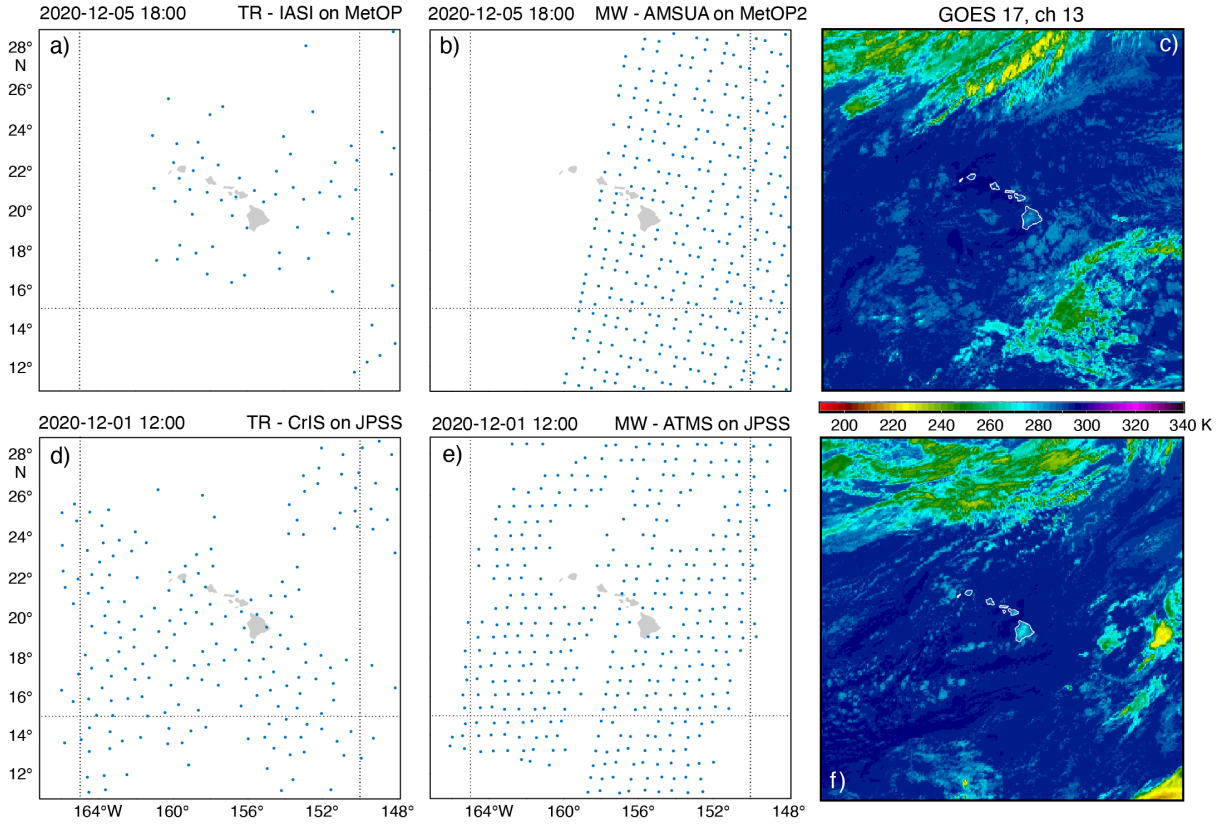

Fig. 4: FOVs locations on Dec. 05, 2020 at 1800 UTC0 UTC for (a) TR from IASI on MetOP platforms and (b) MW from AMSU-A on MetOP-2 and (c) corresponding InfraRed GOES 17 image (channel 15, cloud top temperature); FOVs location on Dec. 1, 2020 at 1200 UTC0 UTC for (d) TR from CrIS on JPSS and (e) MW from ATMS on JPSS and (f) corresponding Infra-Red GOES 17 image (channel 15, cloud top temperature).

Three cycling assimilation experiments were configured. The first solely assimilates conventional observations and is hereafter referred to as the control (CO) experiment. The second experiment also assimilates the high-resolution infrared data in the form of TR and is hereafter referred to as the TR experiment. Finally, the third experiment also assimilates MW radiances and is hereafter referred to as FULL/TRMW experiment. Each experiment consists

of a 3-h cycling system that starts on November 20th at 0000 UTC and ends on December 18th, at 1200 UTC, 2020. Each experiment is cold-started every three days and comprises nine full cycles (nine cold start forecasts). Given the typical overpass times over Hawai‘i of polar orbiting satellites carrying hyperspectral sensors, TRs are usually available for the 0000/1200 UTC (CrIS on *Suomi* NPP/*NOAA-20*) and 0600-0900/1800-2100 UTC (IASI on *MetOPs*) assimilation times. MicroWave radiances are available for the same times as the TRs are because *Suomi NPP/NOAA-20* carries both CrIS and ATMS, and *MetOP-A/B/C* carries both IASI as hyperspectral sensor and AMSU-A and MHS as MW sensors. Moreover, MW sensors are available on the NOAA constellation (NOAA-18/19) with AMSU-A. Figure 4 shows the geographical distributions of the TR and MW observations that were successfully assimilated from the sensors (IASI and AMSU-A) on board of *MetOP* and the sensors (CrIS and ATMS) on board JPSS. Aside from the difference in assimilated observations, the three experiments were otherwise configured identically. Only the observations within ±1 h of the analysis time were assimilated and all observations were assumed to be valid at analysis time.

As for radiance assimilation, the Community Radiative Transfer Model (CRTM, Weng et al. 2005) is used and a Variational Bias Correction (VarBC, Auligné et al. 2007; Auligné and McNally 2007; Auligné 2007) applied. In particular, the VarBC is cold started[3] on the first cycle of the sequence where radiance assimilation happens (Nov 20, 2020 at 0600 UTC) and is updated throughout the experiment timeframe. A radiance data thinning of 80 km is applied during assimilation to avoid potential correlations between adjacent observations (Ochotta et al. 2005) and maintain consistency with the TR thinning. Figure 5 shows the effects of the applied VarBC to one of the ATMS channels for one of the assimilation times. A similar behavior is found for all used channels and times. On the other hand, Fig. 6 seems to suggest that the TRs might not need a bias correction scheme and similar behavior is found for all assimilated eigenvectors. While VarBC is an important step in satellite radiance data assimilation, it can be challenging to perform, more so in limited area models, as it requires a deep understanding of the underlying predictors and anchoring observations (Auligné et al. 2007). VarBC also requires a spin up time in order to produce meaningful predictors[4].

[3] VarBC needs bias predictor statistics (mean and standard deviation) that depend on the model configuration chosen and assimilated radiances. The first-time radiances are assimilated, VarBC is cold started (i.e., biases are unknown). Afterword, during any future assimilation cycle, VarBC bias predictor coefficients are updated if enough independent anchoring observations exist. (https://www2.mmm.ucar.edu/wrf/users/wrfda/Docs/radiance_userguide_v1.pdf, page 13)

[4] https://www2.mmm.ucar.edu/wrf/users/wrfda/Docs/radiance_userguide_v1.pdf, page 11

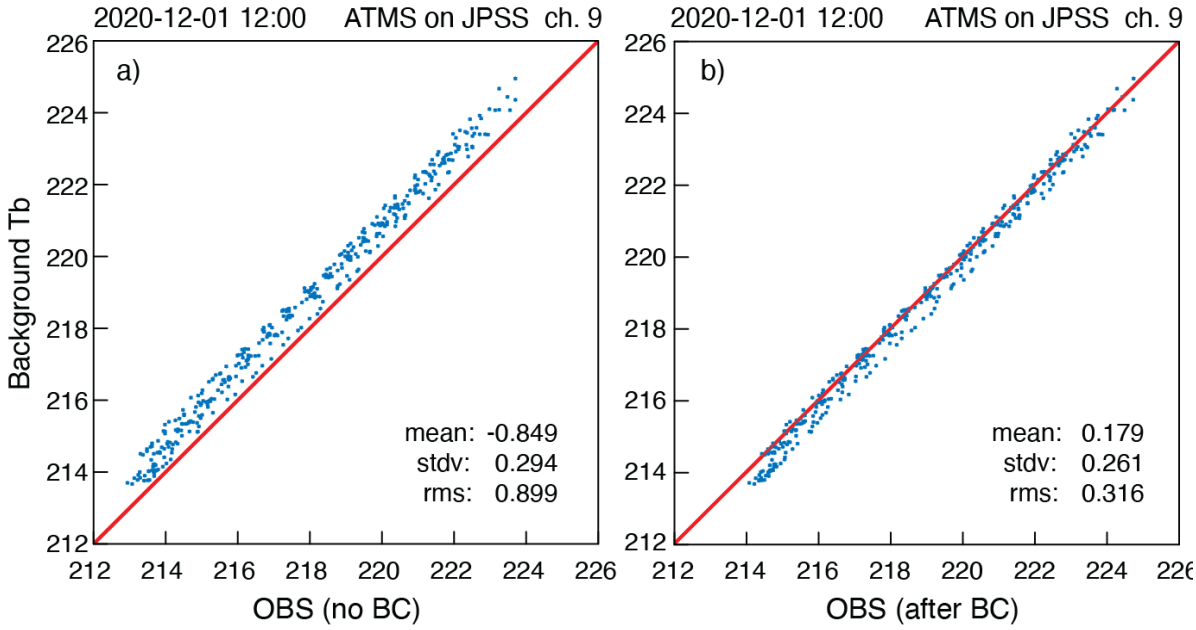

Fig. 5: Scatterplots of observed versus computed brightness temperatures for JPSS ATMS channel 9, before (a) and after (b) bias correction.

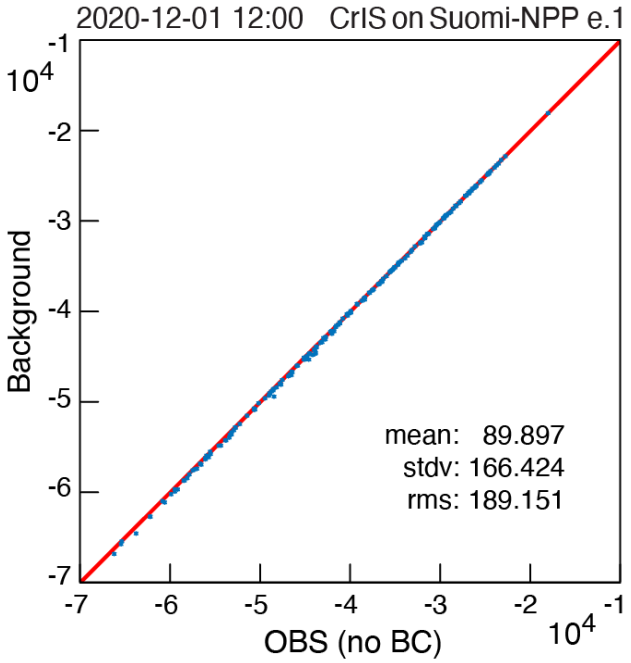

Fig. 6: Scatterplot of observed versus computed TRs for Suomi NPP CrIS, corresponding to the first eigenvector. No BC is applied nor is one needed.

As polar-orbiting satellite positions vary temporally, data from a given satellite may be unavailable over the computational domain at a particular analysis time. Given the typical overpass times of the satellite platforms involved in this experiment, the cycling times with less or near nil satellite data availability are the 0300 and 1500 UTC (Fig. 7). For the TR experiment the number of assimilated statistically independent data is (blue bar segments in Fig 7a):

$$N_{TR}=N_{TR\_FOVS} * N_{eigen} \quad (1)$$

where N_{TR_FOVS} is the number of assimilated TR FOVs and N_{eigen} is the number of assimilated eigenvectors that passed the internal/local quality check procedure. The number of assimilated eigenvectors can change during the various cycles depending on local conditions.

For the TRMW experiments the total number of assimilated data is (red bar segment in Fig. 7a):

$$N_{TRMW}=N_{TR'}+N_{MW\_FOVS} * N_{MW\_ch} \quad (2)$$

where $N_{TR'}$ is the number of assimilated TRs data (which could differ from the case when only TR are assimilated, N_{TR}), N_{MW_FOVS} is the number of assimilated MW FOVs, and N_{MW_ch} is the number of actively assimilated MW channels. The amount of satellite data flowing into the TRMW experiment is broken down by sensor in Fig. 7b, while Fig. 7c shows the difference $\Delta N(TR)=N_{TR}-N_{TR'}$. In general, the number of TRs assimilated changes slightly through the various assimilation cycles depending on whether MW radiances are also assimilated. However, the difference is large on the first TR assimilation cycle. In fact, while the experiments start with a cold start forecast on Nov 20, 2020 at 0000 UTC, only conventional observations and no satellite data of any kind are assimilated at the following cycle (0300 UTC). At 0600 UTC on Nov 20, 2020 the TRs, which are available for this time frame, are assimilated and not rejected by the WRFDA only in the experiment when MW data are also assimilated. A cycling system needs many observations in order not to diverge. Conventional observations might be too few and sparse in the region of interest, more so at asynoptic times, to realistically constraint a new cycle. The concurrent use of TR and MW seems to kick off the system sooner, highlighting the synergy and complementary nature of these two datasets.

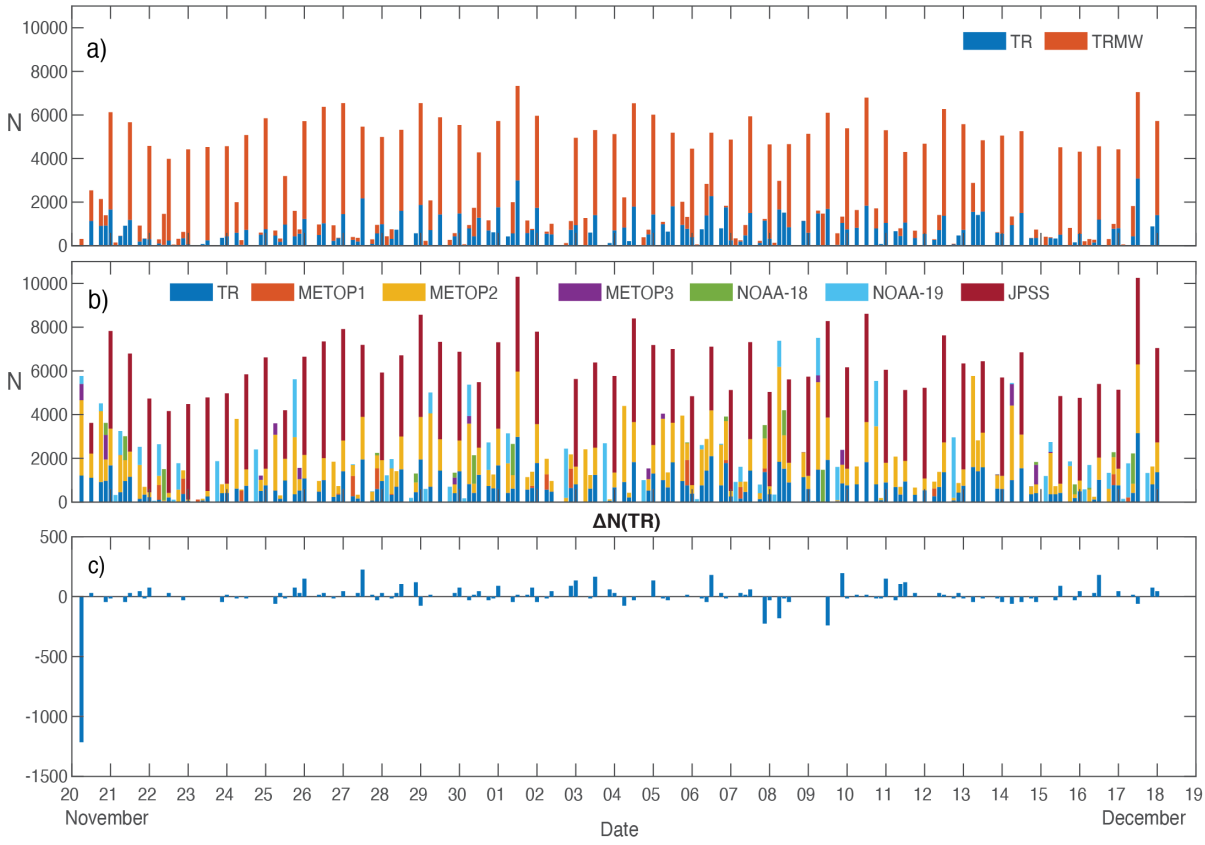

Fig. 7: Number of satellite observations used at each assimilation cycle after passing quality control: a) in the TR (blue bar) and TRMW (red bar) experiments; b) in the TRMW experiment broken down by sensor. c) Difference between the amount of TR data assimilated in the TR experiment minus the amount of TR assimilated in the TRMW experiment.

The meteorological conditions during the experiment time frame included periods of fair weather, characterized by the effect of ridging and subsidence, alternating with frontal systems, and/or short-wave troughs, drifting through the modeled domain. The last week of November and the first week in December 2020 were particularly active with a series of troughs or short-wave troughs quickly passing through. A deeper marine boundary layer, with increased moisture and cloud cover characterized this period. In contrast, average weather conditions were rather benign during the timeframe from December 8 to 15, with at most very weak and shallow fronts skimming across the northern portion of the model domain. A rather sharp upper-level trough impacted the area in mid-December (15-17), followed again by fair weather for the Christmas' holidays, and ahead of a short-wave trough that developed in a cut-off low over and east of the Big Island on the 27th and 28th of December. The role of the meteorological conditions on the results will be discussed in the results section.

4. Evaluation Methodology

Evaluation of the experiments performance is carried out in reference to two different analyses datasets: (i) the NCEP GFS analyses (NCEP 2015), and (ii) the European Centre for Medium-Range Weather Forecasts (ECMWF) Integrated Forecast System (IFS) CY41r2 High-Resolution Operational Analysis and Forecasts (ECMWF 2016). The GFS and ECMWF analyses are used to evaluate all the WRF forecast hours validating the synoptic times for which the global analyses are available. The ECMWF analyses, being the result of an independent model and different data assimilation system, provide complementary insights in the validation procedure. Moreover, the two global analysis datasets have different spatial resolutions. The GFS analyses are available at 0.25-degree resolution, which corresponds to ~25 km horizontal resolution at the experiment latitudes. On the other hand, the operational ECMWF analyses, in which variables are originally available as spectral coefficients, are transformed at RDA to a regular 5120 longitude by 2560 latitude N1280 Gaussian grid, which results in an ~9 km (0.08 degrees) horizontal resolution. Validation using analyses with different spatial resolutions provides insights on the model ability to reproduce processes on different spatial scales.

The WRF model outputs from each forecast cycle are interpolated from their original resolution (lat/lon regular, 4.5 km x 4.5 km grid) onto both the GFS and ECMWF grids to allow for a comparison on a common scale. The WRF model output and global analyses are also interpolated on common pressure levels. Because WRF cycling frequency is 3 hours, and the global models' analyses are available at synoptic times only, the 6 and 12-h WRF forecasts from the 0000, 0600, 1200 and 1800 UTC WRF cycles and the 3 and 9-h forecast from the 0300, 0900, 1500 and 2100 UTC WRF cycles can be validated against global model analyses (Fig. 8).

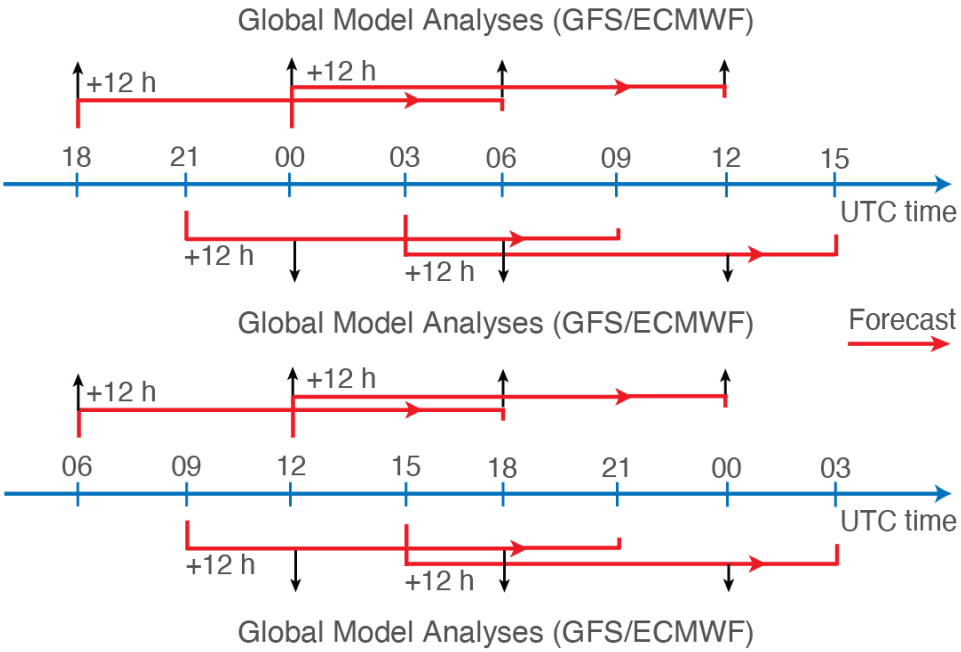

Fig. 8: Verification strategy for 6 and 12-h forecasts from 1800, 0000, 0600 and 1200 UTC cycles and 3 and 9-hour forecasts from the 2100, 0300, 0900, 1500 UTC. The cycles can be validated against GFS and ECMWF analyses.

Statistics can then be built, aggregating the predicted variables of interest temporally and spatially over some or all the analyses time and on various levels. To objectively quantify the differences in the three experiments, the following statistical measures are used. The BIAS, RMSE, and bias corrected RMSE ($RMSE_b$) are defined as:

$$\text{BIAS} = \sum_{i=1}^{N} \frac{F_i - O_i}{N} \tag{3}$$

$$RMSE = \sqrt{\sum_{i=1}^{N} \frac{(F_i - O_i)^2}{N}} \tag{4}$$

$$RMSE_b = \sqrt{\sum_{i=1}^{N} \frac{\left[(F_i - O_i) - \overline{(F_i - O_i)}\right]^2}{N}} \tag{5}$$

where, F and O refer to the forecast and observed field under investigation, respectively.

The ECMWF analyses at 0000 and 1200 UTC are the results of a sophisticated data assimilation system comprising more real time observations than those at 0600 and 1800 UTC (Lean et al. 2020; Haseler, 2004) and are, therefore, of higher quality than the 0600 and 1800 UTC analyses. For the sake of simplicity, only the 0000 and 1200 UTC analyses are considered when using ECMWF in this validation study.

Additional verification is performed against the radiosondes' data available from the two Hawaii locations (PHTO, Hilo; PHLI, Līhu'e). The t_0+3, t_0+6, t_0+9 and t_0+12 hour forecast vertical profiles for temperature, relative humidity, and water vapor from the closest grid point to the two radiosondes' location are extracted and compared against the corresponding sonde's observations. Radiosonde soundings consist of a series of point measurements of atmospheric pressure, temperature, humidity, and wind at high resolution taken from a balloon borne instrument package as it ascends through the atmosphere. The advection of the ascending sonde by the wind results in the sonde drifting away from the launching location. The model vertical profiles instead represent the meteorological variables through the vertical column over the model grid point closest to the radiosonde location. To allow for a fairer comparison, the radiosonde profiles are interpolated on the model vertical grid.

The main statistical measure used is the bias corrected RMS (eq.5). For validation against global model analyses, the results are stratified by forecast hour and averaged throughout all the forecast cycles (0000 UTC, 0300 UTC… et cetera). This validation does not include the model analysis time (t_0) as radiosondes are also included in the CO assimilation and, therefore, are not an independent set of observations for this particular time.

5. Results

Most of the results discussed hereafter refer to the effect of satellite assimilation on the moisture field relative humidity (RH). In fact, the assimilation of TRs has a greater impact on the characterization of the water vapor distribution than the temperature field because of the higher spatial variability of the water vapor concentrations and independence of the water vapor field from temperature and pressure (A2020).

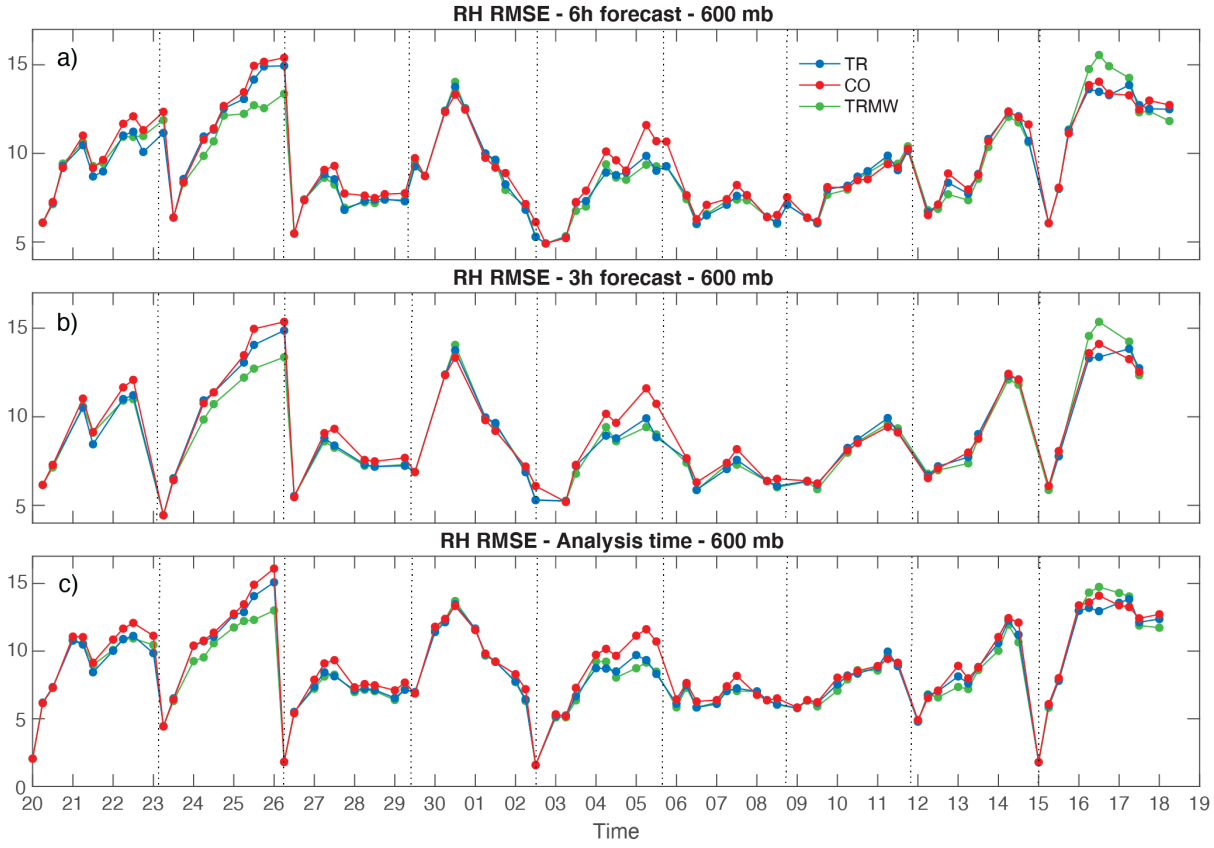

Fig. 9: The RMSEb of the 6 h (a), 3 h (b) forecast RH, and at analysis time (c) at 600 mb, over a one month period. Graphs show CO (red line), TR, (blue line), and FULL, TRMW (green line) experiments. GFS analyses are used as reference field in the statistics.

The RH bias corrected RMSE (RH $RMSE_b$, eq. 5) time series for each of the three month-long experiments are calculated considering the RH WRF forecasts at the validating time and chosen level (600 and 800 hPa), and the corresponding RH GFS analyses (Fig. 9 and 10). The grid points falling on land are excluded from the calculations because of the relatively coarse resolution of the global model when compared to island dimensions and complex topography. The statistics are averaged over the WRF domain and stratified by validation date and time. The time series highlight the consecutive cycling experiments: a cycle is the results of eight WRF simulations, each providing a 12h long forecast. The statistics show decreasing absolute forecast accuracy with an increasing cycling number (that is, away from each cold start) within the same cycle, but an increasing relative accuracy (lower $RMSE_b$) for both the TR and TRMW experiments compared to the control run where only conventional observations are ingested. As expected, the improvement in the forecast accuracy performance is cumulative through each 3-day model cycle and accentuated even more on the 800 hPa level (Fig. 10). It is also consistent throughout most of the month-long timeframe, although there are periods when the

differences between experiments are quite small (assimilation cycles 4, 7 and 8). These periods correspond to spells of relatively calm weather in the area of interest and, therefore, the additional assimilated data might not add much more information into the custom analyses.

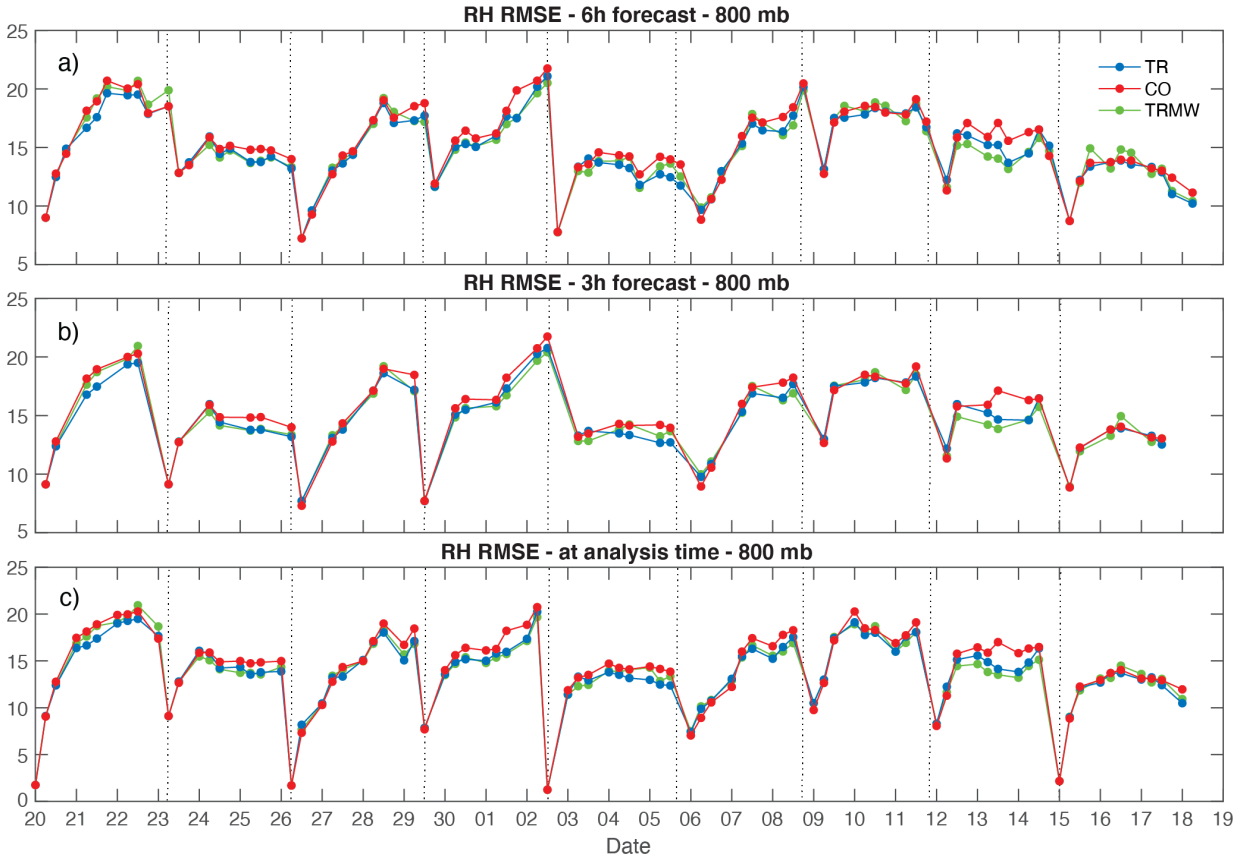

Fig. 10: RMSEb of the 6 h (a), 3 h (b) forecast RH and at analysis time (c) at 800 mb, over a month: CO (red line), TR, (blue line), and FULL, TRMW (green line) experiments are shown. GFS analyses are used as reference field in the statistics.

In the second assimilation cycle (Nov. 23–26), the TRMW experiment performs better than the control and the TR experiment, at the 600 hPa level. In all the other cycles where TR outperforms the control run, the TRMW experiment either performs equally or slightly worse. Both the 3-h and 6-h forecasts show a similar impact.

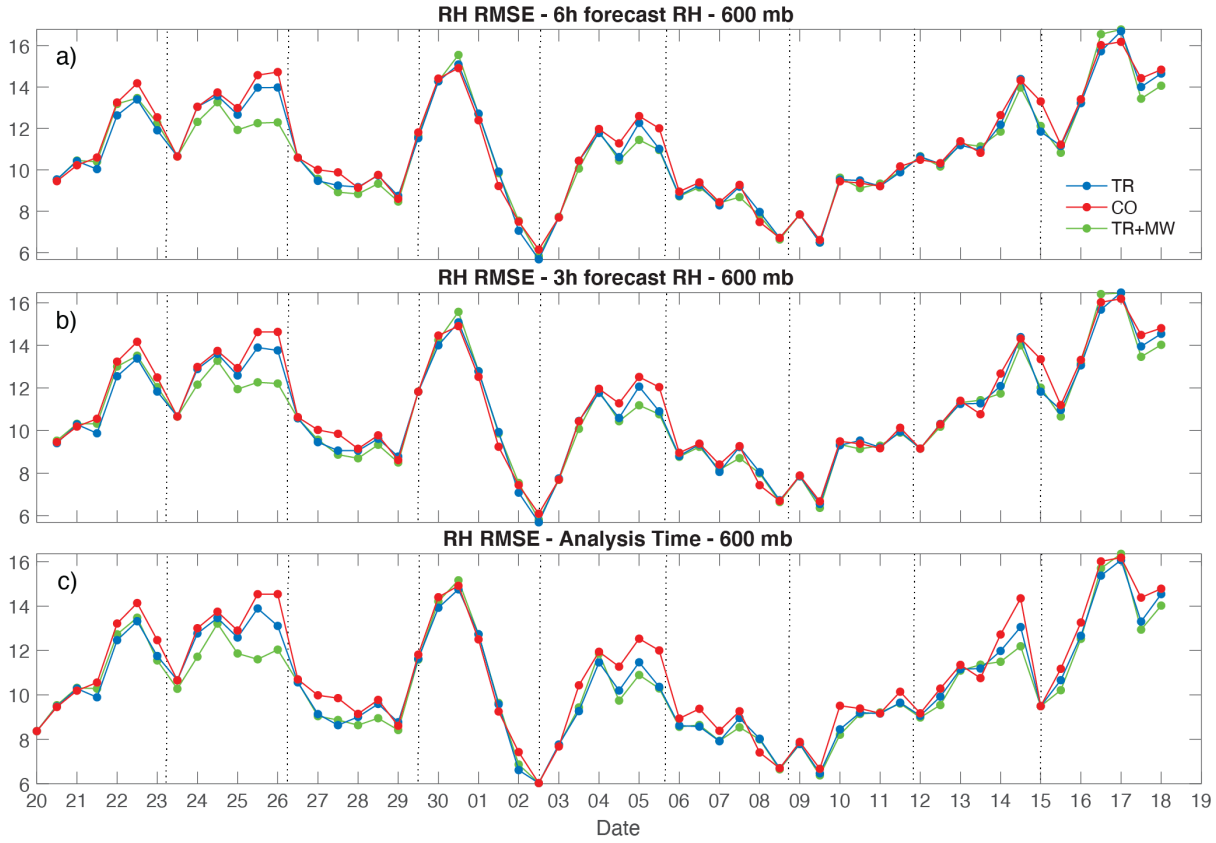

Fig. 11: $RMSE_b$ of the 6 h (a), 3 h (b) forecast RH and at analysis time (c) at 600 mb, over a one month period. Graphs show CO (red line), TR, (blue line), and FULL, TRMW (green line) experiments. ECMWF analyses are used as reference field in the statistics.

These results can be explained by the underlying amount of information provided by the TRs, which are a compressed form of the information content in thousands of channels from the hyperspectral sensors. Although MWs are available in larger numbers in terms of FOVs, they represent a smaller number of satellite channels (~ of tens or less). Also, TRs for a single FOV are statistically independent, whereas MW channels for a single FOV are not. In fact, the retrieval process through Mirto provides a representation of the information embedded in thousands of correlated channels in form of uncorrelated quantities (TRs). On the other hand, there are fewer MW channels but they are still correlated among themselves because of their broad and overlapping weighting functions. When the ECMWF is used as true state in the $RMSE_b$ calculation in equation 5, the RH $RMSE_b$ time series for the 600 hPa level (Fig. 11) shows very similar results to those obtained when GFS is used in the validation. On the other hand, a larger improvement is found on the 800 hPa level (Fig. 12) when TR are assimilated, both with and without MW. This finding is true for all analyzed forecast hours 0, 3, and 6. This particular result is encouraging for several reasons.

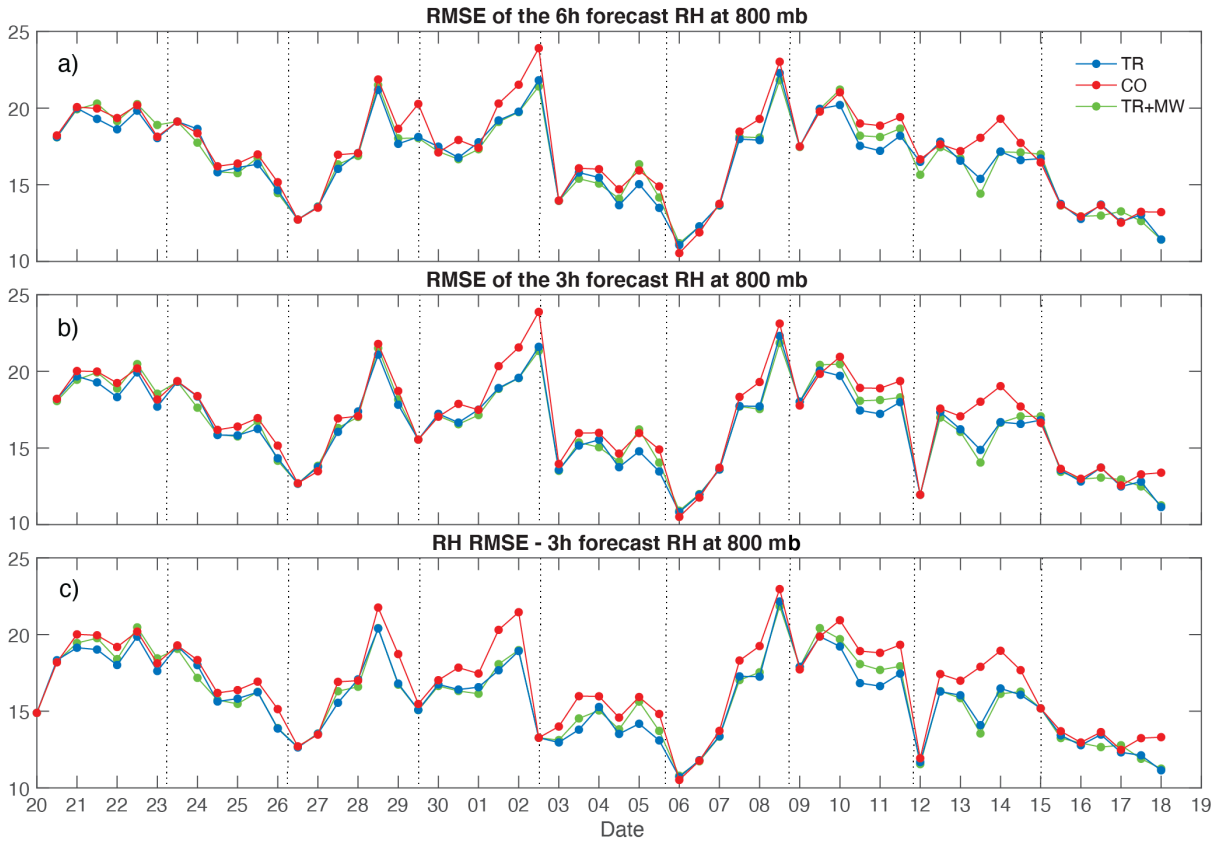

Fig. 12: $RMSE_b$ of the 6 h (a), 3 h (b) forecast RH and at analysis time (c) at 800 mb, over a one month period. Graphs show CO (red line), TR, (blue line), and FULL, TRMW (green line) experiments. ECMWF analyses are used as reference field in the statistics.

The improvement at 800 hPa is likely due to a refinement in the vertical definition of the trade wind inversion. An increased model performance against higher resolution analyses (ECMWF) points to better custom WRDA analyses. Smaller scale moisture structures that would usually be smoothed out by the coarser GFS analyses resolution are captured instead. The custom analysis from the assimilation of TRs improves with respect to an independent and higher resolution analysis provided by ECMWF. On the other hand, validating against ECMWF analyses versus GFS analyses shows similar gains in the middle/higher levels of the atmosphere as meteorological fields are naturally smoother in the free atmosphere, being further removed from the effects of turbulence induced by surface friction.

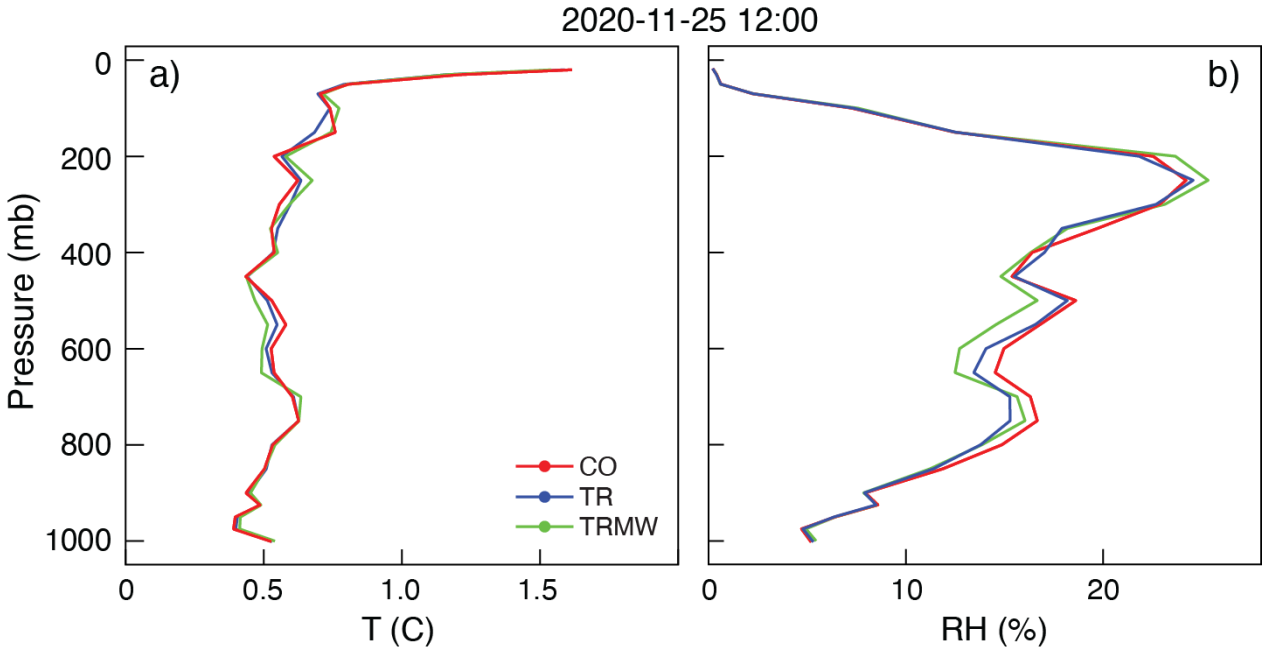

Fig. 13: Vertical profiles of $RMSE_b$ for the 3 h forecast temperature (a) and RH (b) on Nov. 25 2020 at 1200 UTC for the CO experiment (red line), TR experiment (blue line), and TRMW experiment (green line). The GFS is used as reference field in the statistics.

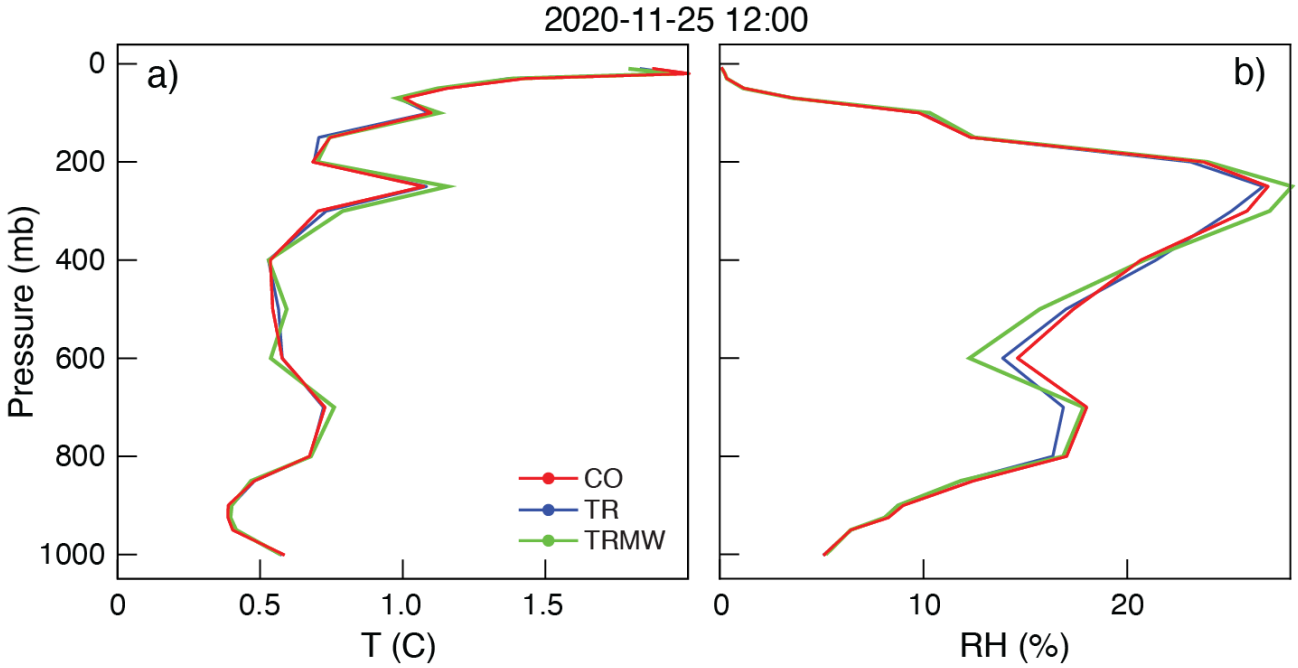

Fig. 14: Vertical profiles of $RMSE_b$ for the 3 h forecast temperature (a) and RH (b) on Nov. 25 2020 at 1200 UTC for the CO experiment (red line), TR experiment (blue line), and TRMW experiment (green line). The ECMWF is used as reference field in the statistics

a. Impact of assimilation on vertical profiles

Vertical profiles of $RMSE_b$, for temperature and relative humidity, averaged throughout the model domain, are also analyzed (Figs. 13 and 14). Given all the possible statistical stratifications (e.g., variable, analysis type, forecast hour, and cycling time) it would be too lengthy to show and discuss all of them here. Both the TR and TRMW experiment show an increase in the 3 h forecast accuracy in the moisture field between 900 and 300 hPa when the GFS is used as the reference field (Fig. 13b). On the other hand, the impact of assimilating both sources of data on the temperature field is very small (Fig. 13a). Figure 14 shows the same but when ECMWF analysis is used as the reference field and the results are similar. Very similar results are also found for all the analyzed profiles/cases: the assimilation of TR alone and both TR and MW improves the 3, 6 and 12 h forecast accuracy in the middle atmosphere, from about 850 hPa to 300 hPa. Also, the larger impact of the TR assimilation is found in the lower portion of this range, in the atmospheric layer from 800 hPa to 600 hPa. Figure 15 shows three more cases during the time from Nov. 25 at 1800 UTC to Nov 26 at 0600 UTC. This time period corresponds to the end of the second assimilation cycle. Again, the largest impact from TR assimilation is found in the lower portion of the middle atmospheric layers. On the other hand, MW assimilation has a large impact in the 600 to 300 mb, complementing the lack of TRs at these levels. TR availability during this cycle is low (Fig. 7) in comparison to the rest of the timeframe, likely due to increased cloud coverage.

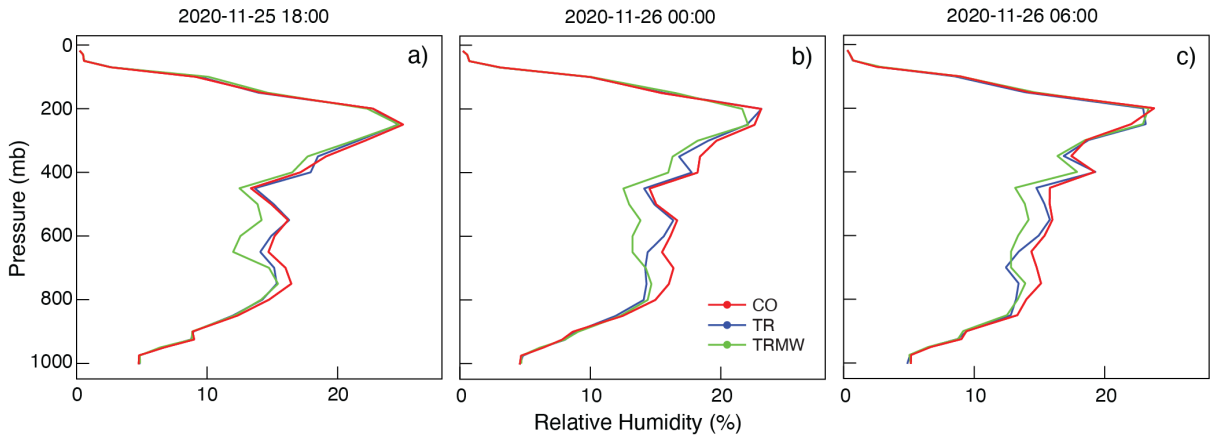

Fig. 15: Vertical profiles of $RMSE_b$ for the: (a) 6 h forecast started on Nov. 25 at 1200 UTC; (b) 3 h forecast started on the Nov. 25 at 2100 UTC; and c) 6 h forecast started on Nov. 26 at 0000 UTC. The GFS is used as the reference field in the statistics.

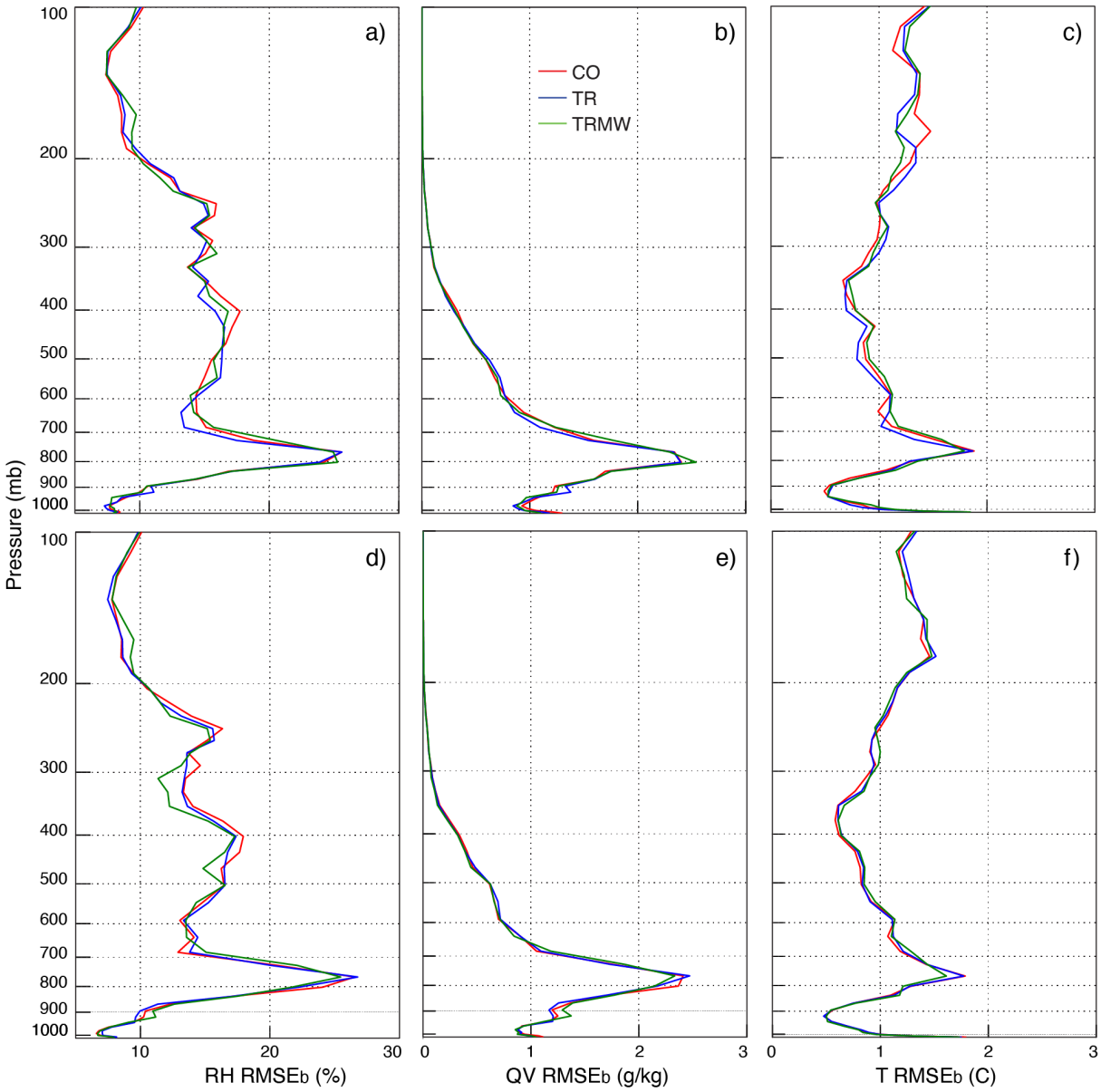

Fig. 16: Vertical profiles of $RMSE_b$ for the 3 h RH (a), Qv (b) and T (c) forecast, and 6 h RH (a), Qv (b) and T (c) forecast throughout the entire experiment (Nov. 20–Dec. 20, 2020). Radiosonde data are used as the reference field for model validation. The statistical sample comprises 107 forecasts. Cold start model runs are not included in the statistics.

Validation against radiosondes observations is summarized in Fig. 16 for the t_0+3h and t_0 +6h forecasts. Results from this analysis are consistent with what was found in our validation against global model analyses: on average, both the TR and TRMW RH forecasts outperform the CO experiment in the middle atmosphere, from about 850 hPa to about 350 hPa. Moreover, the TR experiment provides slightly better results at t_0+3h than the TRMW experiment. Differences between experiments in terms of temperature RMSEb are generally quite small. However, while they seem negligible at t_0+6h, small positive impact is found at t_0+3h,

particularly in the highest atmospheric levels (100 to 200 hPa) where a warm bias is often found in the model initial conditions when compared to observational data (Cucurull and Anthes, 2014). The improvement from assimilating TR and TR and MW together is still discernible in the t_0 +6h RH forecasts.

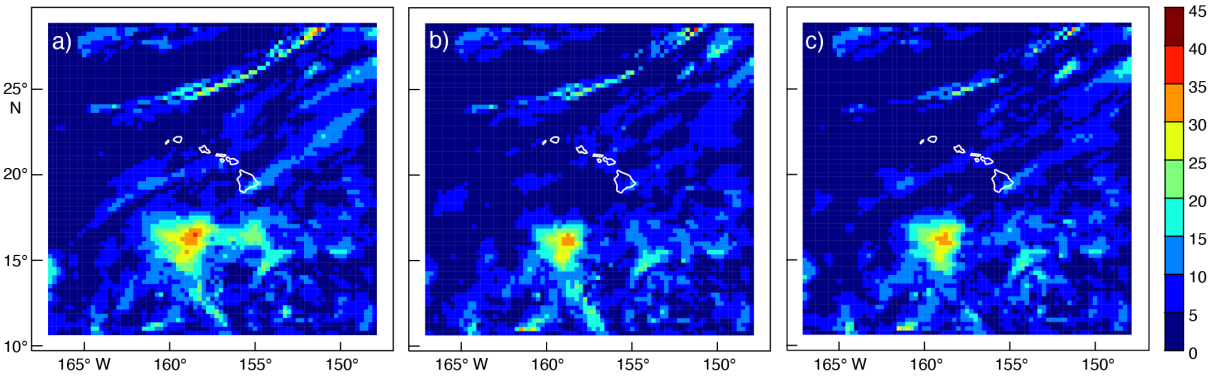

Fig. 17: $RMSE_b$ for the 3 hour 600 mb RH forecasts started at 09000 UTC in the timeframe spanning from 02 Dec to 5 Dec. (5^{th} cycle) when the GFS is used as reference field in the statistics for experiment: a) CO; b) TR; and c) TRMW.

b. Impact of assimilation on horizontal synoptic structures

The assimilation of TR alone and both TR and MW improves the 3-h forecast accuracy on the 600 hPa level both when verifying against GFS (Fig. 17) and ECMWF analyses (Fig. 18). These figures, which includes all the 3-h forecasts started at 0900 UTC in the fifth assimilation cycle, shows how the areas of larger RMSEs shrank for the TR and TRMW experiments versus the control experiment. There is significant reduction everywhere, however, two areas stand out: i) the area interested by the passage of a weak frontal system, north of the islands; ii) a large area in the Big Island's wake, in the southwestern quadrant of the model domain. The reduction of the former is perhaps an indication of a better handle by the forecast model of the location and timing of the frontal passage during those simulations. The area of greater errors in the wake of the Big Island is associated with the turbulent shifting of a convergence zone that results from the flow splitting around the high volcanos that make up the island. The higher errors are a reflection of sub-grid-scale processes that are not well captured by the global models but are captured by the higher resolution WRF model. Assimilation of TR alone or TR and MW results in a reduction of this forecast error. The smoother features in Fig. 18 reflect ECMWF's higher resolution grid.

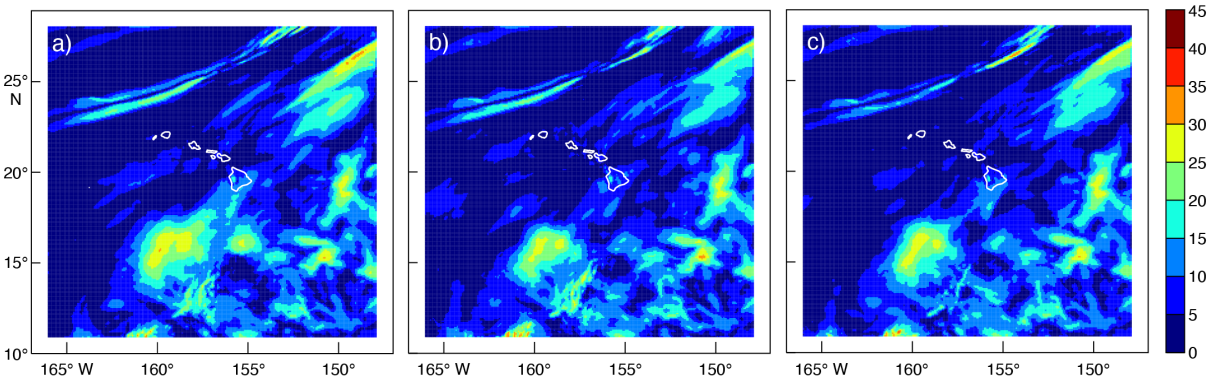

Fig. 18: RMSEb for the 3-hour 600 mb RH forecasts started at 0900 UTC in the timeframe spanning from 02 Dec to 5 Dec. (5th cycle) when the ECMWF is used as reference field in the statistics for experiment: a) CO; b) TR; and c) TRMW.

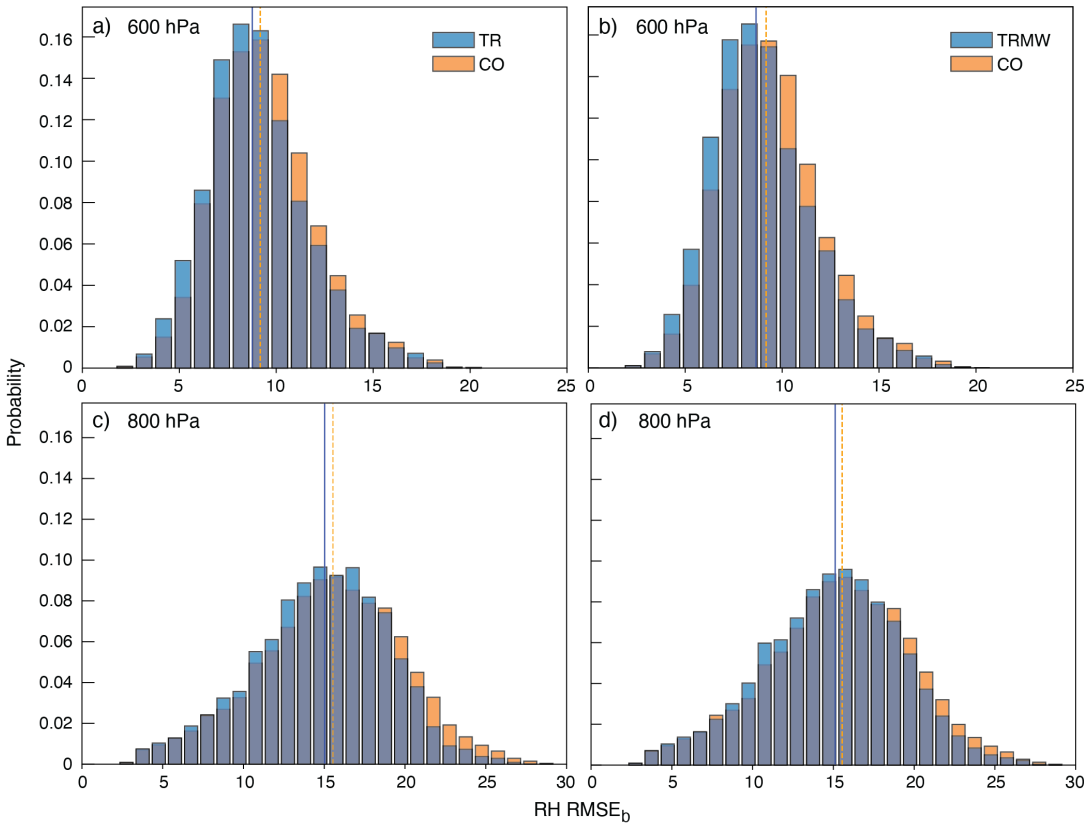

Fig. 19: RH RMSE$_b$ distribution for the 3-hour forecasts started at 0900 UTC throughout the entire experiment (Nov. 20 through Dec. 20, 2020) at 600 hPa, when the GFS is used as reference field in the statistics: a) comparison between TR and CO at 600 hPa; b) comparison between TRMW and CO at 600 hPa; c) comparison between TR and CO at 800 hPa; d) comparison between TRMW and CO at 800 hPa.

Figures 19 and 20 summarize these results when the entire experiment timeframe is considered. The RH $RMSE_b$ distribution for all the 3-h forecasts started at 0900 UTC in the month-long experiment and the 600 hPa and 800 hPa levels are shown using histograms. When both GFS and ECMWF analyses are used in the validation procedure, the distributions corresponding to forecasts where either TR or TR and MW were assimilated shift toward lower values, indicating a significant overall improvement in predicting RH in the middle atmospheric levels. The overall improvement is larger when ECMWF is used as reference field on the 800 hPa level (Fig. 20c, d). This reinforces the conclusion made earlier those improvements at this level are larger due to better placement of the trade wind inversion.

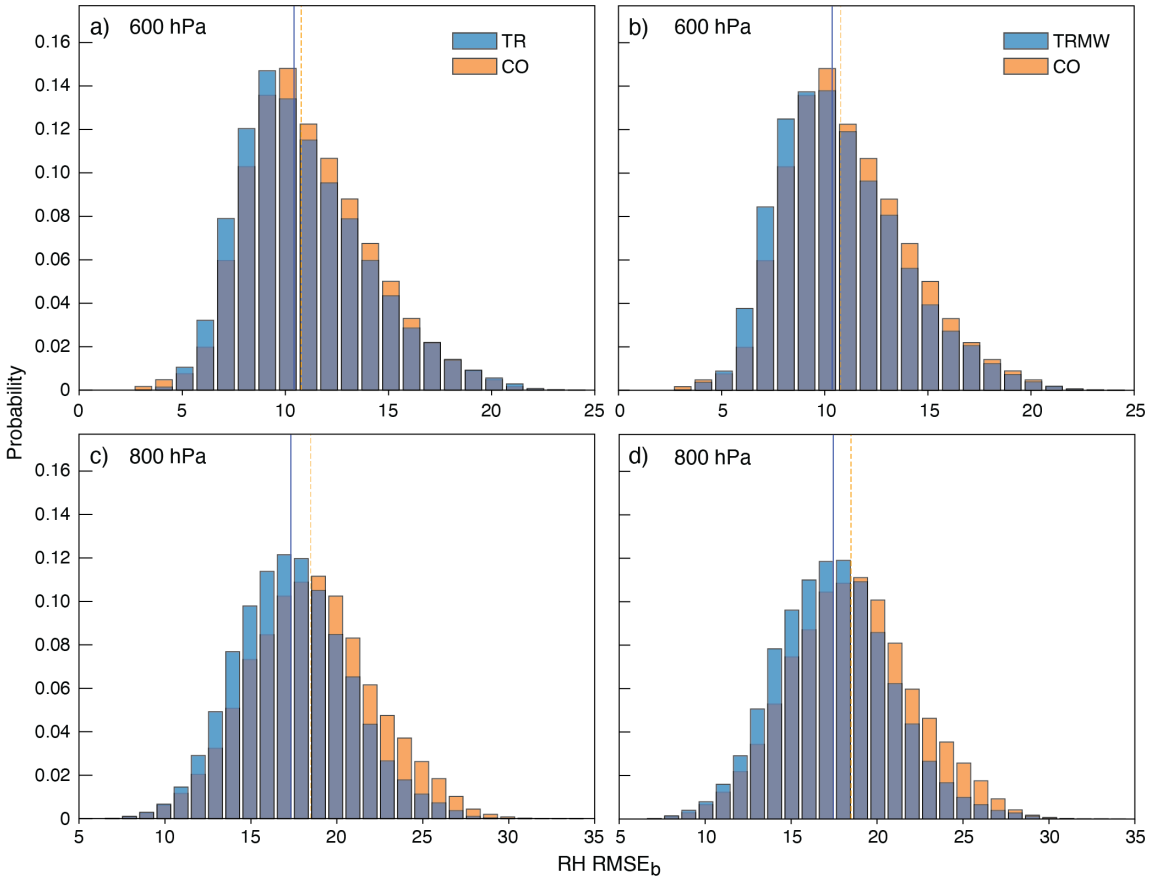

Fig. 20: Fig. 20. RH $RMSE_b$ distribution for the 3-hour forecasts started at 0900 UTC throughout the entire experiment (Nov. 20 through Dec. 20, 2020) at 600 hPa, when the ECMWF is used as reference field in the statistics: a) comparison between TR and CO at 600 hPa; b) comparison between TRMW and CO at 600 hPa; c) comparison between TR and CO at 800 hPa; d) comparison between TRMW and CO at 800 hPa.

6. Conclusions and Discussion

This work is an extension of A2020 and presents the results of an assessment of the impact of TR assimilation into the WRF modeling system in a month-long experiment over the Central North Pacific Area. TRs are generated using ‘‘Mirto’’ (Antonelli et al. 2017) while a modified version of the WRFDA model is used to ingest TRs. Three cycling assimilation experiments were configured: (i) control (CO) experiment, where only conventional observation are assimilated; (ii) TR assimilation experiment, where high-resolution infrared data in the form of TR are also assimilated; (iii) and a TRMW experiment, where MW radiances are also ingested. Each experiment consists of a 3-h cycling system that starts on November 20th at 0000 UTC and ends on December 18th, at 1200 UTC, 2020. Each experiment is cold-started every three days and comprises nine full 3-day cycles. Each 3-day cycle contains 24 forecasts, initialized every three hours. For the purpose of this study, each forecast is 12-h-long. Both the GFS and ECMWF analyses, available at synoptic times, were used to evaluate the impact of the new assimilation approach on the accuracy of the WRF forecasts. Radiosonde profiles available within the domain of interest are also used in the validation.

A comparison between model analyses and forecasts is performed on the horizontal and vertical grid each GCM analysis is defined on and the $RMSE_b$ is the main statistical measure used in the statistical analyses. For validation against radiosondes, observed profiles are interpolated on the model vertical grid over the model grid point closest to the sonde launching locations. Again, the $RMSE_b$ is used as main statistical measure.

This study confirms that assimilation of hyperspectral data has a larger impact on water vapor distribution than on the temperature field. The results of the statistical analysis can be summarized as follows.

- The positive results presented in this study seem to suggest that there is no need for Bias Correction. This implies that: (i) the a-priori information embedded in the retrievals is removed quite efficiently by the inversion process; and (ii) the hyperspectral radiances are radiometrically accurate.

- TR assimilation is ultimately more comparable to single profile assimilation than radiance assimilation.

- RH $RMSE_b$ timeseries on 800 and 600 hPa show a decreasing absolute forecast accuracy with the increasing cycling number, within the same 3-day cycle, but an

increasing relative accuracy (lower $RMSE_b$) for both the TR and TRMW experiments compared to the control run where only conventional observations are ingested.

- In most cycles, forecast accuracy after TR assimilation outperforms the control forecast accuracy. The forecast's accuracy after both TR and MW are assimilated either performs equally or slightly worse that assimilation only of TRs, but for one 3-day cycle when the number of available TRs was relatively small (due to higher cloud coverage).

- The improvement is even greater when ECMWF output is used as the reference field in the statistics particularly at the 800 mb level, for the shorter 3h forecasts, and at analysis time.

- The analysis of the RH $RMSE_b$ vertical profiles indicates that the assimilation of TR alone and combined assimilation of TR and MW improves the 3, 6, and 12 h forecast accuracy in the middle atmosphere from about 850 hPa to 300 hPa, both when the GFS and the ECMWF are used as reference field in the statistics. Also, a larger impact of the TR assimilation is found in the atmospheric layer from 800 hPa to 600 hPa.

- The RH $RMSE_b$ cumulated over time and analyzed on the modeled domain at 800 hPa and 600 hPa shows that forecasts after TRs assimilation perform better in predicting the timing and location of horizontal synoptic structures like fronts passing by. Also, the forecast's error is reduced in the convergence zone, which results from the flow splitting around the Big Island (Hawai'i). Moreover, the spatial RH $RMSE_b$ distribution calculated through the entire experiment timeframe shows significant improvement (lower $RMSE_b$) when TRs are assimilated both alone (best results) and in combination with MW. Results are even better when the independent ECMWF analyses are used as reference field in the statistics, particularly at the 800 mb level.

- The analysis of the $RMSE_b$ vertical profiles obtained when radiosondes are used as reference field indicates that the assimilation of TR, alone or in combination with MW, has a small positive impact, compared with assimilation of CO only, on the 3- and 6-h RH forecasts in the middle atmosphere from about 850 hPa to about 350 hPa. Moreover, a small positive impact is also found in the 3-h temperature forecast at the highest atmospheric levels (100 to 200 hPa) where a warm bias is often found in the model initial conditions when compared to observational data.

In addition to the positive impact of this new assimilation approach on the accuracy of both the analyses and forecasts, once the diagnostic system is equipped with the TR assimilation module, assimilation of TRs is easier than radiance assimilation for the following reasons.

- A radiative transfer model is not needed.
- The information content is compressed into a limited number of parameters (< 20). In contrast, direct radiance assimilation requires fine tuning many factors, most of them sensor related.
- The observation operator comes with the TR data, making the assimilation independent of the sensor.

Discussion

The dominant impact of the TRs on the forecast accuracy can be explained by the underlying amount of information provided by the TRs: the information content contained in thousands of channels from the hyperspectral sensors is highly and efficiently compressed into a limited number of uncorrelated parameters. On the other hand, MW radiances, although available in larger numbers in terms of FOVs, underlie a small number or satellite channels, that are likely correlated, because of their broad and overlapping weighting functions. Nevertheless, because of the lack of TRs information in cloudy area (so far), assimilation of MW radiances can prove complementary to TRs assimilation for those cases where cloud coverage can be an issue because MWs can penetrate clouds. The combination of IR TR and MW radiances seems to confirm their complementary nature in terms of spatial coverage, vertical resolution, and cloud impact mitigation. Having Mirto soundings available over the clouds would add additional useful information to the forecast system.

Both the assimilation of TRs and MWs results in a higher forecast accuracy in predicting the distribution of the water vapor in the middle atmosphere. The assimilation of TRs improves the model performance in the lower portion of the middle atmosphere (800–700 hPa) and this is an even clearer takeaway from the statistical analysis carried out against the ECMWF analyses. This result is encouraging for several reasons. The improvement at 800 hPa is likely due to a refinement in the vertical definition of the trade-wind inversion. An increased model performance against higher resolution analyses (ECMWF) points out to better custom WRDA analyses. Smaller scale moisture structures that would be smoothed out by the coarser GFS analyses resolution are captured instead. The custom analysis from the assimilation of TRs is

improved with respect to an independent and higher resolution analysis provided by ECMWF. Validating against ECMWF analyses versus GFS analyses shows similar gains in the middle/higher levels of the atmosphere as meteorological fields are naturally smoother in the free atmosphere, being further removed from the effects of turbulence induced by surface friction.

When forecasts and initial analyses are compared against the higher spatial resolution of ECMWF analyses, the diagnostic and forecasts are able to capture small weather features and improve the placement of the trade wind inversion. This latter is particularly important for the central North Pacific region for several reasons: i) the trade wind inversion produces a layer of warm temperatures and dry air in the mid-levels of the atmosphere due to the sinking and adiabatic warming of the mid-level air, which inhibits deep convection and produces a stable lapse rate that inhibits formation of thunderstorms and tropical cyclones; ii) the trade wind inversion height and strength is correlated with rainfall intensity and distribution, particularly on the windward slopes of the Hawaiian islands (Esteban and Chen, 2008); iii) an accurate prediction of the trade wind inversion height provides helpful guidance to the MKWC forecaster in assessing the weather at the summit of Maunakea (Lyman et al. 2020).

Hyperspectral instruments on polar orbiting satellites provide global coverage with high spatial and temporal resolution and can be an important resource for regions where conventional observations are lacking, such as over the open ocean and the Arctic. In fact, these data are widely assimilated in the NWP (Baker et al. 2005). Research shows that the ECMWF forecast errors are largest over the Arctic and far fewer MW observations are assimilated during winter than in summer in the ECMWF system, especially in regions covered by snow and sea ice (Lawrence et al. 2019). TR assimilation holds particular promise in these data sparse areas of the globe.

The authors of this study are currently pursuing operational implementation of the WRF cycling system with TR and MW assimilation both over the Pacific and the Arctic. Another area of active research is calculation and assimilation of TRs in cloudy regions, which will be particularly important over the Arctic. A future goal is to make TR assimilation available to other operational models such as NCEP's GFS and the Navy's new Neptune model through implementation in the JEDI framework (https://www.jcsda.org/jcsda-project-jedi).

Acknowledgments.

Thanks go to Nancy Hulbirt for help with the figures and May Izumi for her support to the manuscript editing. We acknowledge high-performance computing support from Cheyenne (doi: 10.5065/D6RX99HX) provided by NCAR's Computational and Information Systems Laboratory (CISL), sponsored by the National Science Foundation. We thank the Research Data Archive (CISL) for conventional MW radiance observations, GFS and ECMWF analyses and forecast data, and the NOAA CLASS archive for CrIS, VIIRS and IASI level 1 data availability. We would also like to acknowledge the Cooperative Institute for Meteorological Satellite Studies (CIMSS) for their Community Satellite Processing Package (CSPP), which was used to process all the data into EDRs and Level1C.

This research was supported by the Office of Naval Research under ONR Award N00014-18-1-2166.

Data Availability Statement.

The data underlying this article will be shared on reasonable request to the corresponding author. The NCEP PREBUFR format data are available in real time via the NCEP web-server (https://www.nco.ncep.noaa.gov/pmb/products/gfs/, NCEP/NWS/NOAA/U.S. Department of Commerce, 2008) and archived as NCEP ADP Global Upper Air and Surface Weather Observations, at the Research Data Archive (RDA) at the National Center for Atmospheric Research (NCAR), Computational and Information Systems Laboratory (CISL), Boulder, CO (available online at https://doi.org/10.5065/Z83F-N512). Microwave radiance data are available in real time via the NCEP web server (https://www.nco.ncep.noaa.gov/pmb/products/gfs/, NCEP/NWS/NOAA/U.S. Department of Commerce 2009) and archived as NCEP GDAS Satellite Data, (BUFR at the RDA (NCAR, CISL), Boulder, CO (available online at https://doi.org/10.5065/DWYZ-Q852). The European Centre for Medium-Range Weather Forecasts (ECMWF, 2016) Integrated Forecast System (IFS) CY41r2 High-Resolution Operational Analysis and Forecasts are archived at the NCAR/CISL, Boulder, CO (available online at https://doi.org/10.5065/D68050ZV). The GFS analyses and forecasts are available in real time via the NCEP web-server (https://www.nco.ncep.noaa.gov/pmb/products/gfs/, NCEP/NWS/NOAA/U.S. Department of Commerce, 2015) and archived as NCEP GFS 0.25-degree global forecast grids historical archive at the RDA (NCAR, CISL), Boulder, CO (available online at

https://rda.ucar.edu/datasets/ds084.1). The Level 1 data from both CrIS (Han et al. 2012) and IASI sensors, along with VIIRS (NOAA 2013) data are available from the NOAA, Comprehensive Large Array-data Stewardship System (CLASS). Radiosonde data are available online at the Dept. of Atmospheric Sciences of the University of Wyoming, College of Engineering (http://weather.uwyo.edu/upperair/sounding.html).

REFERENCES

Antonelli P., T. Cherubini, T. Auligne, L. Bernardini, S. Businger, and F. Marzano, 2015: The potential of METEOSAT Third Generation (MTG) InfraRed Sounder (IRS) level 2 product assimilation in a very short-range numerical weather forecast model. EUMETSAT Final Rep., 79 pp.

Antonelli, P., T. Cherubini, R. Lyman, G. Giuliani, H. Revercomb, and S. Businger, 2017: Regional retrieval processor for direct broadcast high-resolution infrared data. *J. Appl. Meteor. Climatol.*, **56**, 1681–1705, https://doi.org/10.1175/JAMC-D-16-0144.1.

Antonelli, P., T. Cherubini, S. Businger, S. de Haan, P. Scaccia, and J. Moncet, 2020: Regional assimilation system for transformed retrievals from satellite high-resolution infrared data. *J. Appl. Meteor. Climatol.*, **59**, 1171–1193, https://doi.org/10.1175/JAMC-D-19-0203.1.

Auligné, T., A. P. McNally, and D. P. Dee, 2007a: Adaptive bias correction for satellite data in a numerical weather prediction system. *Quart. J. Roy. Meteor. Soc.,* **133**, 631–642, https://doi.org/10.1002/qj.56.

Auligné, T., and A. P. McNally, 2007b: Interaction between bias correction and quality control. *Quart. J. Roy. Meteor. Soc.,* **133**, 643–653.

Auligné, T., 2007c: An objective approach to modeling biases in satellite radiance assimilation: application to AIRS and AMSU-A. *Quart. J. Roy. Meteor. Soc*., **133**(628), 1789–1801, https://doi.org/10.1002/qj.145.

Barker, D. M., W. Huang, Y.-R. Guo, A. J. Bourgeois, and Q. N. Xiao, 2004: A three-dimensional variational data assimilation system for MM5: Implementation and initial results. *Mon. Wea. Rev*., **132**, 897–914.

Barker, D. M., and Coauthors, 2012: The Weather Research and Forecasting Model's Community Variational/Ensemble Data Assimilation System: WRFDA. *Bull. Am. Meteorol. Soc*., **93**, 831–843, https:// doi.org/10.1175/BAMS-D-11-00167.1.

Baker, N. L., T. F. Hogan, W. F. Campbell, R. L. Pauley, and S. D. Swadley, 2005: The impact of AMSU-A radiance assimilation in the U.S. Navy's Operational Global Atmospheric Prediction System (NOGAPS). Marine Meteorology Division, Naval Research Laboratory, Memo. NRL/MR/7530–05-8836, 22 pp.

Businger, S., R. McLaren, R. Ogasawara, D. Simons, and R. J. Wainscoat, 2002: Starcasting. *Bull. Am. Meteorol. Soc*., **83**, 858–871, https://doi.org/10.1175/1520-0477(2002)083,0858:S.2.3.CO;2.

Cherubini, T., S. Businger, C. Velden, and R. Ogasawara, 2006: The impact of satellite-derived atmospheric motion vectors on mesoscale forecasts over Hawaii. *Mon. Wea. Rev*., **134**, 2009-2020, doi:10.1175/MWR3163.1.

Cherubini, T., S. Businger, and R. Lyman, 2011: An operational perspective for modeling optical turbulence. In *Seeing Clearly: The Impact of Atmospheric Turbulence on the Propagation of Extraterrestrial Radiation*, S. Businger and T. Cherubini (eds.), VBW Publishing, 165–182.

Cherubini, T., R. Lyman, and S. Businger, 2021: Forecasting seeing for the Maunakea observatories with machine learning. *Mon. Not. R. Astron. Soc.*, **509**(1), 232–245, https://doi.org/10.1093/mnras/stab2916.

Corrigan, T. J., and S. Businger, 2021: The anatomy of a series of cloud bursts that eclipsed the U.S. rainfall record. *Mon. Wea. Rev*., **150**(4), 753–773, https://doi.org/10.1175/MWR-D-21-0028.1.

Cucurull, L., and R. A. Anthes, 2014: Impact of infrared, microwave, and radio occultation satellite observations on operational numerical weather prediction. *Mon. Wea. Rev*., **142**(11), 4164–4186, https://doi.org/10.1175/MWR-D-14-00101.1.

Dee, D. P., 2005: Bias and data assimilation. *Quart. J. Roy. Meteor. Soc.*, **131**(613), 3323–3343.

DeHaan S., G.-J. Marseille, and P. De Valk, 2015: The potential of METEOSAT Third Generation (MTG) InfraRed Sounder (IRS) level 2 product assimilation in a very short range numerical weather forecast model. EUMETSAT, technical report.

Dudhia, J., 1989: Numerical study of convection observed during the winter monsoon experiment using a mesoscale two-dimensional model. *J. Atmos. Sci.,* **46**(20), 3077–3107, https://doi.org/10.1175/1520-0469(1989)046<3077:NSOCOD>2.0.CO;2.

European Centre for Medium-Range Weather Forecasts, 2016: ECMWF IFS CY41r2 High-resolution operational forecasts. Research Data Archive at the National Center for Atmospheric Research, Computational and Information Systems Laboratory, Boulder, CO, https://doi.org/10.5065/D68050ZV (updated monthly).

Esteban, M. A., and Y.-L. Chen, 2008: The impact of trade wind strength on precipitation over the windward side of the Island of Hawaii. *Mon. Wea. Rev.,* **136**, 913–928, https://doi.org/10.1175/2007MWR2059.1.

Eyre, J. R., 2007: Progress achieved on assimilation of satellite data in numerical weather prediction over the last 30 years. Seminar on Recent Developments in the Use of Satellite Observations in Numerical Weather Prediction, Shinfield Park, Reading, United Kingdom, ECMWF, https://www.ecmwf.int/sites/default/files/elibrary/2008/9341-progress-achieved-assimilation- satellite-data-numerical-weather-prediction-over-last-30-years.pdf.

Eyre, J. R., 2016: Observation bias correction schemes in data assimilation systems: A theoretical study of some of their properties. *Quart. J. Roy. Meteor. Soc*., **142**, 2284–2291, https://doi.org/10.1002/qj.2819.

Eyre, J.R., S. J. English, and M. Forsythe, 2019: Assimilation of satellite data in numerical weather prediction. Part I: The early years. *Quart. J. Roy. Meteor. Soc*., **146**, 49–68, https://doi.org/ 10.1002/qj.3654.

Han, Y., S. Qiu, Shuang, and NOAA JPSS Program Office, 2012: NOAA JPSS Cross-track Infrared Sounder (CrIS) Science Sensor Data Record (SDR) from IDPS. JPSS-CrIS-SDR. NOAA National Centers for Environmental Information, doi: 10.7289/V59C6VGK.

Haseler, J., 2004: Early-delivery suite. ECMWF Technical Memoranda, 454, http://doi.org/10.21957/f3wtwz0h.

Hong, S., and J. Lim, 2006: The WRF Single-Moment 6-Class Microphysics Scheme (WSM6). *J. Korean Meteor. Soc.*, **42**, 129–151.

Janjic, Z. I., 2002: Nonsingular implementation of the Mellor-Yamada level 2.5 scheme in the NCEP Meso model, NCEP Office Note, No. 437, 61 pp, https://repository.library.noaa.gov/view/noaa/11409.

Lawrence, H., N. Bormann, I. Sandu, J. Day, J. Farnan, and P. Bauer, 2019: Use and impact of Arctic observations in the ECMWF Numerical Weather Prediction system. *Quart. J. Roy. Meteor. Soc*., **145**, 3432–3454, https://doi.org/10.1002/qj.3628.

Lean, P., E. V. Holm, M. Bonavita, N. Bormann, A. P. McNally, and H. Jarvinen, 2020: Continuous data assimilation for global numerical weather prediction. *Quart. J. Roy. Meteor. Soc.*, **147**, 27–288., https://doi.org/10.1002/qj.3917.

Lyman, R., T. Cherubini, S. Businger, 2020: Forecasting seeing for the Maunakea Observatories. *Mon. Not. R. Astron. Soc.*, **496**(4), 4734–4748, https://doi.org/10.1093/mnras/staa1787.

Mlawer, E. J., S. J. Taubman, P. D. Brown, M. J. Iacono, and S. A. Clough, 1997: Radiative transfer for inhomogeneous atmosphere: RRTM, a validated correlated-k model for the longwave. *J. Geophys. Res.*, **102** (D14), 16663–16682.

Migliorini, S., 2012: On the equivalence between radiance and retrieval assimilation. *Mon. Wea. Rev.*, **140**, 258–265, https://doi.org/10.1175/MWR-D-10-05047.1.

——, C. Piccolo, and C. Rodgers, 2008: Use of the information content in satellite measurements for an efficient interface to data assimilation. *Mon. Wea. Rev.*, **136**, 2633–2650, https://doi.org/10.1175/2007MWR2236.1.

National Centers for Environmental Prediction, National Weather Service, NOAA, and U.S. Department of Commerce, 2008: NCEP ADP Global Upper Air and Surface Weather Observations (PREPBUFR format). Research Data Archive at the National Center for Atmospheric Research, Computational and Information Systems Laboratory [data set], https://doi.org/10.5065/Z83F-N512.

National Centers for Environmental Prediction/National Weather Service/NOAA/U.S. Department of Commerce, 2009: NCEP GDAS Satellite Data 2004-continuing. Research Data Archive at the National Center for Atmospheric Research, Computational and Information Systems Laboratory, Boulder, CO, https://doi.org/10.5065/DWYZ-Q852 (updated daily).

National Centers for Environmental Prediction/National Weather Service/NOAA/U.S. Department of Commerce, 2015: NCEP GFS 0.25 Degree Global Forecast Grids Historical Archive. Research Data Archive at the National Center for Atmospheric Research, Computational and Information Systems Laboratory, Boulder, CO, https://doi.org/10.5065/D65D8PWK (updated daily).

NOAA National Centers for Environmental Information, 2013: VIIRS Climate Raw Data Record (C-RDR) from Suomi NPP, Version 1. NCEI DSI 3658_01. NOAA National Centers for Environmental Information, doi: 10.7289/V57P8W90.

Ochotta, T., C. Cebhardt, D. Saupe, and W. Wergen, 2005: Adaptive thinning of atmospheric observations in data assimilation with vector quantization and filtering methods. *Quart. J. Roy. Meteor. Soc.*, **131**, 3427–3437, https://doi.org/10.1256/qj.05.94.

Skamarock, W. C., J. B. Klemp, J. Dudhia, D. O. Gill, D. Barker, M. G. Duda, X. Huang, W. Wang, and J. G. Powers, 2008: A description of the Advanced Research WRF Version 3 (No. NCAR/TN-475+STR). University Corporation for Atmospheric Research, doi: 10.5065/D68S4MVH.

Simmons, A. J., and A. Hollingsworth, 2002: Some aspects of the improvement in skill of numerical weather prediction. *Quart. J. Roy. Meteor. Soc.*, **128**, 647–677.

Wang, Y., J. He, Y. Chen, and J. Min, 2021: The potential impact of assimilating synthetic microwave radiances onboard a future geostationary satellite on the prediction of Typhoon Lekima using the WRF model. *Remote Sens*., **13**, 886, https://doi.org/10.3390/rs13050886.

Weng, F., Y. Han, P. Van Delst, Q. Liu, and B. Yan, 2005: JCSDA community radiative transfer model (CRTM). In *Proc. 14th Int. ATOVS Study Conf.*, pp. 217–222.

Zapotocny, T. H., J. A. Jung, J. F. Le Marshall, and R. E. Treadon, 2008: A two-season impact study of four satellite data types and rawinsonde data in the NCEP Global Data Assimilation System. *Wea. Forecasting,* **23**, 80–100.

Zhang, C., and Y. Wang, 2017: Projected future changes of tropical cyclone activity over the western North and South Pacific in a 20-km-mesh regional climate model. *J. Climate*, **30**, 15, 5923–5941, https://doi.org/10.1175/JCLI-D-16-0597.1.